Temperature and poroelasticity of sedimentary rocks

Thermal conductivity, permeability and temperature effects on stiffness and strength properties of sandstones

Tobias Orlander

PhD Thesis

Department of Civil Engineering
2018

DTU Civil Engineering Report 403

DTU Civil Engineering
Department of Civil Engineering

TEMPERATURE AND POROELASTICITY OF SEDIMENTARY ROCKS

Thermal conductivity, permeability and temperature effects on stiffness and strength properties of sandstones

Tobias Orlander

PhD Thesis

April 2018

PREFACE

This thesis is submitted as a partial fulfilment of the requirements for the PhD degree at Technical University of Denmark (DTU). The PhD-project was carried out from 2014 to 2018 at the Department of Civil Engineering under the supervision of Professor Ida Lykke Fabricius and Assistant professor Katrine Alling Andreassen. DTU, Innovation Fund Denmark, Maersk Oil and DONG Energy funded the project. The experimental work was carried out partly in Denmark at DTU and at the consultancy, Geo, and partly in Germany at German Research Centre for Geosciences, GFZ Potsdam in co-operation with Senior Researcher Dr. Harald Milsch, during a series of visits in 2016 and 2017.

This is a paper-based thesis comprising a synthesis and three journal paper manuscripts (Orlander et al., I, II and III), where the first is accepted and the latter two submitted. Titles of accepted and submitted manuscripts are given in Appendix I. Supplementary texts, completed during the PhD study, include two published conference papers and three conference abstracts. Titles of supplementary texts are given in Appendix II.

Unless otherwise indicated, the PhD student performed the experimental work using the laboratory facilities at DTU, Geo or GFZ Potsdam. Mercury injection capillary pressure curves however, were measured by John C. Troelsen, DTU. X-Ray spectra and electron microscope images were analyzed by Ida L. Fabricius.

Kongens Lyngby, April 30, 2018

Tobias Orlander

SUMMARY

Increasing interest in the exploration for High Pressure High Temperature (HPHT) petroleum reservoirs and for geothermal reservoirs calls for theoretical and experimental knowledge of temperature effects on sedimentary rocks. Sandstone is one class of sedimentary rocks of interest to both industries, and the physical understanding of temperature effects on mechanical properties as well as governing characteristics of fluid and heat transfer in sandstones can be essential for industrial success.

With respect to temperature influence on elasticity and strength, sandstone samples from three wells in the central North Sea Basin were studied. The samples were collected from depths exceeding 5 km and in-situ temperatures above 170°C. This is relevant for drilling operations, because the success and safety of a drilling operation rely on accurate estimates of the subsurface effective stress field. Failure to take into account the significant temperature effects on both stiffness and strength properties may lead to inaccurate stress estimates and thus cause risk. With the intention of experimentally quantifying temperature effects on rock stiffness and strength properties, the three sandstones were tested in the dry state at temperatures from ambient to in-situ (170°C). Results show a material stiffening during increasing temperature, reflected in both static and dynamic elastic moduli. These observations can be attributed to thermal expansion of the constituting mineral particles by two mechanisms of different magnitude depending on the boundary conditions. Likewise, strength parameters derived from measurements of shear failure at ambient and in-situ temperature show strengthening with temperature. This observation may also be attributed to thermal expansion of constituting minerals. The effective stress field modelled from the conventional Biot equation implies isothermal conditions, but for non-isothermal conditions it is possible to include thermoelastic theory. Results of interpreting logging data by using the conventional as well as the non-isothermal Biot equation to estimate the subsurface effective stress in a North Sea well show that the non-isothermal Biot equation predicts a smaller effective stress. Results further indicate the possibility of a neutral effective stress at great depth so that the overburden load may be carried solely by the pore pressure and thus might be floating on the highly overpressured older layers.

Permeability is a key hydraulic property in both petroleum and geothermal engineering and of great interest with respect to sandstones. Commonly, conventional laboratories derive the apparent liquid permeability of core plugs from empirical or semi-empirical corrections to the

gas permeability derived from flow-through experiments. Correcting gas permeability derived from flow-through experiments to the apparent liquid permeability is conventionally denoted Klinkenberg correction. From flow-through experiments, liquid permeability on a series of outcrop sandstones shows good agreement with the apparent liquid permeability from classical Klinkenberg correction of gas permeability obtained at laminar flow conditions and thus compatible with linear Darcy's law. In gas permeability experiments not only Klinkenberg correction is necessary, but also the confirmation of laminar flow so that the linear Darcy equation is valid. For this purpose an estimate of Reynolds number can be done based on apparent pore size as estimated from backscatter electron micrographs. For doing Klinkenberg correction, the number of gas permeability data points can be limited by availability of core material, so estimates of permeability may be based on one or more petrophysical properties, which may not be of hydraulic character. Estimation of permeability from non-hydraulic properties calls for an understanding of the governing petrophysical principles. Results of Nuclear Magnetic Resonance Spectrometry on the sandstone samples used for liquid flow-through experiments show that the largest pores in the sandstones do not form a continuous path and consequently the smaller pores control the overall permeability.

Because of minimal subsurface coring, assessment of depth variations in thermal conductivity is typically limited to applying empirical relations to downhole logging data, but by combining input parameters from the concepts of rock stiffness and permeability, it is possible to establish a new model for thermal conductivity. Provided a given mineralogical composition, the model can estimate formation thermal conductivity as a function of depth using solely parameters quantified through conventional log interpretation. The applicability is demonstrated by comparing measured data with model predictions of thermal conductivity with input from laboratory data of sandstones identical to ones used in permeability studies, as well as logging data from an exploration well of the Gassum Formation near Stenlille, Denmark.

SAMMENFATNING

Stigende interesse for dybe olie-gas reservoirer samt geotermisk energi, hvor fællesnævneren er den høje temperatur i undergrunden, medfører et stigende behov for teoretisk og eksperimentel viden om sedimentære bjergarter. Sandsten er én type af sedimentære bjergarter, som er af interesse for industrien, hvor fysisk forståelse af temperatureffekter på stivhed og styrkeegenskaber og karakteristika for væske og varmetransport kan være bestemmende for den industrielle succes.

Olie og gas reservoirer, begravet under Nordsøen på dybder større end 5 kilometer og ved temperaturer over 170°C, er ofte af sandsten, og det giver anledning til ønske om øget teoretisk og eksperimentel forståelse af temperatureffekter på stivheds- og styrkeegenskaberne. Stivheds- og styrkeegenskaber er knyttet til sikkerheden ved boring, og udeladelse af signifikante temperatureffekter kan lede til usikre estimater af materialeegenskaberne og derved føre til øget risiko ved dybe boringer. For at kvantificere temperatureffekter på stivhed og styrke, blev tre sandsten fra Nordsøen testet ved temperaturer fra stue- til in-situ temperatur. De resulterende statiske og dynamisk stivhedsparametre viser en øget stivhed med stigende temperatur. Dette kan tilskrives termisk udvidelse af de enkelte sandkorn gennem to mekanismer, som er forskellig i størrelsesorden samt bestemt af randbetingelserne. Klassiske styrkeparametre bestemt ved styrkeforsøg foretaget ved stue- samt in-situ temperatur viser øget styrke ved den høje temperatur, Dette tilskrives ligeledes termisk udvidelse af de enkelte sandkorn. Sikkerheden ved dybe boringer er også knyttet til estimater af de effektive spændinger i undergrunden, som til dels er styret af stivhedsegenskaber, hvilket ydermere øger nødvendigheden af viden om temperatureffekter. Modellering af de effektive spændinger ved hjælp af den konventionelle Biot-ligning, forudsætter isotermiske randbetingelser, men hvis termoelastisk teori inkluderes, kan en ikke-isotermisk ligning formuleres. Bruges den ikke-isotermiske ligning i en boring i det dybe Nordsøbassin, viser resultaterne effektive spændinger, der er lavere end de konventionelt beregnede. Dette indikerer at ved stor dybde, er spændingerne neutrale, således at post-Triassic lag i princippet kan tænkes at flyde på ældre lag, som er under overtryk.

I undergrundsindustrien inden for både olie/gas og geotermi er permeabilitet en vigtig hydraulisk egenskab. Konventionelle laboratorier afleder almindeligvis den tilsyneladende væskepermeabilitet ud fra empiriske eller semi-empiriske korrektioner af gaspermeabilitet målt ved gennemstrømningsforsøg på kerneprøver. Konventionelt betegnes dette som Klinkenberg-

korrektion. Klinkenberg-korrektionens brugbarhed blev her eftervist på en række sandsten, hvor den tilsyneladende væskepermeabilitet (Klinkenberg-permeabilitet) afledt af målt gaspermeabilitet blev sammenlignet med direkte målt væskepermeabilitet. Det viste sig her væsentligt at sikre sig laminar gasstrømning, således at Darcy's ligning gælder. Dette kan gøres ved at estimere Reynolds tal ud fra porestørrelse som observeret ved mikroskopi af tyndslib.

Mængden af kernemateriale er generelt stærkt begrænset, hvilket resulterer i få permeabilitetsmålinger, og fører til nødvendigheden af estimater baseret på en eller flere petrofysiske egenskaber, som ikke direkte er af hydraulisk karakter. Dette kræver omfattende fysisk forståelse af de styrende petrofysiske egenskaber. For at illustrere, at de større porer ikke udgør en kontinuert pore, og at mindre porer styrer den overordnede permeabilitet, blev Kozeny's ligning i kombination med kernemagnetiske resonansmålinger på en række sandstenprøver anvendt til at udlede permeabilitetsbidrag fra hver enkelt porestørrelse, og resultaterne bekræfter, at et bidrag fra de største porer er unødvendigt for at matche den målte væskepermeabilitet.

Ydermere, som følge af minimal adgang til kernemateriale, vurderes dybdevariationer i termisk ledningsevne ofte ud fra log-data kombineret med empiriske relationer. Ved at anvende koncepter fra stivhed og permeabilitet til kvantificering af strukturen i sandsten kan en nyetableret model estimere termisk ledningsevne under forudsætning af kendt mineralogi. Modellen anvender udelukkende parametre fra standard logging og konventionel logtolkning. Den etablerede model benytter afledte parametre til at kvantificere tværsnittet for varmeoverførsel i enkeltkomponenter (faste og flydende), og inden for de fysiske grænser af et enhedsvolumen, opsummeres den samlede varmeoverførsel for at udlede et teoretisk udtryk for den effektive termiske ledningsevne. Ved at anvende laboratoriemålinger på de samme sandsten, som blev brugt til undersøgelsen af permeabilitet, samt brug af log-data fra Gassum sandstenen, blev den modellerede termiske ledningsevne sammenlignet med målt termisk ledningsevne. Resultaterne viser, at termisk ledningsevne fra den nyetablerede model er i bedre overensstemmelse med målinger end andre konventionelle modeller især for log-data.

ACKNOWLEDGEMENT

First and foremost, I would like to express my appreciation to both my principal supervisor Professor Dr. Ida Lykke Fabricius as well as my co-supervisor Assistant Professor Katrine Alling Andreassen for all the help.

I will thank students and collaborators for support with experimental, scientific, as well as written work. Many people have contributed with help and advice during my studies and all deserve my gratitude. From Geo I will thank all the people in the laboratory as well as the workshop. In the laboratory at the Technical University of Denmark, Department of Environmental Engineering, I will thank Sinh H. Nguyen and Hector O. A. Diaz and from the laboratory at the Department of Civil Engineering Carolyn E. Skouenby and Ditte J. Valentin. Special thanks go to John C. Troelsen for the colossal help and many cheerful talks and to Niels Nielsen Foged for mentoring.

I will thank Dr. Harald Milsch at GFZ for collaboration and kind support during my stays in Potsdam, Germany.

I will thank the innovation fund Denmark and respectively the former Maersk Oil and DONG energy for financial support (Grant number 113-2012-1).

All my current and former colleagues at the Department of Civil Engineering have my deepest gratitude for their help and for making the years good ones.

Finally, I will thank Nina Agnete Orlander and Emma Agnete Orlander for their patience and support as my wife and daughter respectively.

LIST OF PUBLICATIONS

Thesis contributions

Orlander et al., I: Orlander, T., Andreassen, K.A., Fabricius, I.L, 2018, Effect of temperature on the subsurface stress and stiffness of sandstones from the deep North Sea Basin, submitted, Geophysics.

Orlander et al., II: Orlander, T., Milsch, H., Fabricius, I.L, 2018, Comparison of gas, Klinkenberg and liquid permeability - controlling pore size as defined from NMR and Kozeny's equation, submitted, Geophysics.

Orlander et al., III: Orlander, T., Adamopoulou, E., Asmussen, J.J., Marczyński, A.A., Milsch. H., Pasquinelli. L., Fabricius, I.L., 2018, Thermal conductivity of sandstones from Biot's coefficient, accepted, Geophysics.

Additional contributions

Orlander, T., Enemark, K.D., Andreassen, K.A., Fabricius, I.L, 2017a, Permeability in deep North Sea sandstones as predicted from NMR, Presented at: 4th International Workshop on Rock Physics, June 2017, Trondheim, Norway. The abstract is found in Appendix VII.

Orlander, T., Adamopoulou, E., Asmussen, J.J., Marczyński, A.A., Milsch. H., Pasquinelli. L., Fabricius, I.L., 2017b, Thermal conductivity of sedimentary rocks as function of Biot's coefficient, Proceeding, 6th Biot Conference on Poromechanics 2017, Paris, ASCE.

Orlander, T., Andreassen, K.A., Fabricius, I.L, 2017c, Temperature Effects on Stiffness Moduli of Reservoir Sandstone from the Deep North Sea, Proceeding, 51st US Rock Mechanics/Geomechanics Symposium, American Rock Mechanics Association, 17-106, 2017, San Francisco, US.

Orlander, T., Pasquinelli. L., Fabricius, I.L., 2018a, Using Biot's coefficient in estimation of thermal conductivity of sandstones, SEG International Symposium on Energy Geotechnics 2018, Lausanne, Switzerland.

Orlander, T., Andreassen, K.A., Fabricius, I.L, 2018b, Stiffening and strengthening by increased temperature of dry sandstones from the deep North Sea Basin, EAGE Annual 80th Conference and Exhibition 2018, Copenhagen, Denmark.

TABLE OF CONTENTS

1. INTRODUCTION

Temperature is a common denominator in the increasing industrial interest in exploration for High Pressure High Temperature (HPHT) petroleum reservoirs and the utilization of geothermal reservoirs. This calls for increased theoretical and experimental knowledge with respect to temperature effects on key properties. For this reason the overall scientific goals for this thesis is to 1) provide new knowledge about temperature effects on rock stiffness and rock strength, as well as estimation of the temperature effect on downhole effective stress, and 2) establish a new model for thermal conductivity using contributions from solid and fluid constituents, as quantified from respectively rock stiffness and permeability. This work focus on the properties of sandstone.

The scientific rationales behind 1) and 2) respectively are:

1. As the petroleum industry targets deeply buried HPHT reservoirs in, e.g., the central North Sea, knowledge of temperature effects on the stiffness and strength properties of sedimentary rocks becomes critical. In the North Sea Basin as in other localities, HPHT reservoirs may be not only subject to high temperature and extreme stress-fields but also to high regional overpressure, which in combination give rise to challenges with respect to safety/control of drilling operations as well as to well stability.

   In estimations of the effective stress-field, temperature effects are typically not included, and when associated with the safety during drilling operations inaccurate estimates may pose a risk when targeting HPHT reservoirs. The effective stress according to the classical Biot equation (Biot 1941) is primarily a function of the total stress (subsurface overburden), but also of the magnitude of total stress carried by the pore fluid. Through the effective stress coefficient (Biot's coefficient), the latter depends on the elastic stiffness properties of the rock frame as well as the constituting mineral and consequently temperature effects may influence stiffness properties, and contribute to the effective stress.

   When applying Mohr-Coulomb's failure criteria, temperature effects on parameters of rock strength determined on downhole sampled material or analog outcrop samples are typically not included, and when associated with the danger

of well collapse, temperature effects consequently pose a risk when targeting HPHT reservoirs.

2. Accurate estimates of key formation properties such as thermal conductivity are essential for the industrial success of geothermal engineering. However, decisions on formation suitability from formation properties are typically limited to estimates from downhole logging campaigns, because tools developed for in-situ measurement of thermal conductivity are not yet part of standard logging campaigns. Consequently, prediction of thermal conductivity requires estimates from other downhole parameters.

Scope of study

The rationales in this study are scientifically addressed in separate studies, but concepts are interchangeably applied, giving the relation between studies. Chapter 3 to 6 summarize the primary theoretical framework, results, and conclusions of each study whereas chapter 2 provide a brief overview of the materials used in experimental work. Appendix III provides a brief description of experimental procedures.

For the scientific rationale of 1):

The work concerning temperature effects on subject matters such as subsurface effective stress, rock stiffness, and rock strength is based on Orlander et al., I, Orlander et al., 2017c and Orlander et al., 2018b. The non-isothermal effective stress formulated from combined poro- and thermoelastic theory constitute the theoretical formulation of the mechanisms that control temperature effects on rock stiffness and strength. The possible consequences of including temperature effects on the subsurface effective stress are shown from a North Sea case study. From experiments conducted on a series of sandstone samples from the deep North Sea Basin at temperatures from ambient to in-situ, changes in stiffness and strength properties were investigated and quantified as a function of temperature. Chapters 3 and 4 summarize the work and primary results.

For the scientific rationale of 2):

The work concerning thermal conductivity in sandstones is divided into quantification of contributions to the overall thermal conductivity from fluid and solid constituents

respectively and is based on Orlander et al., II; Orlander et al., III; Orlander et al., 2017a; Orlander et al., 2017b as well as Orlander et al. 2018a. By using concepts from rock stiffness and permeability respectively to quantify contributions to the overall thermal conductivity from solid and fluid constituents, a theoretical model of thermal conductivity with application to sandstone was established. On a series of outcrop sandstones, properties of thermal conductivity, stiffness, and permeability were measured and used for validation of the model prediction. Chapters 5 and 6 summarize the work and primary results.

2. EXPERIMENTALLY STUDIED SANDSTONE MATERIAL

The focus of this thesis is on sandstone material in general, and both downhole-sampled and outcrop sandstone material was experimentally studied. Studies of temperature effects on stiffness and strength properties based on experimental work used downhole-sampled material whereas studies on thermal conductivity and permeability used outcrop samples.

2.1 North Sea sandstones

Downhole sampled sandstone material originates from three North Sea HPHT wells and depths of 4.5 to 5.5 km and in-situ temperatures of approximately 170°C. The wells are denoted as O, H, and C respectively.

As derived from thin section petrography, X-ray diffraction (XRD) and Energy Dispersive X-ray Spectroscopy (EDS), the samples from well O, H, and C contain quartz, feldspar, and phyllosilicates. Detected phyllosilicates include mica (illite) and chlorite. In H and O is calcite detected (Table 2.1). Presence of pyrite and organic matter is detected in sample O (Table 2.1). The presence of calcite is not detected from XRD in sample C but is indicated by chemical analysis of the carbonate content. The content is however only in the order of 1%.

Table 2.1. Mineralogical composition of reservoir material as detected by XRD and EDS.

Well	Quartz	Kali-feldspar	Calcite	Phyllo-silicate	Pyrite	Organic matter (coal)
O	X	X	X	X	X	X
H	X	X	X	X		
C	X	X		X		

X indicated detected presence.

For O samples, Backscatter Electron Micrograph (BSEM) images show quartz and calcite as dominating and load bearing minerals. However, the relative proportion of quartz and calcite vary between samples (Figure 2.1a and b). In addition to quartz and calcite, significant quantities of organic matter (coal) with pyrite is found in some O samples (Figure 2.1a, and c).

BSEM-images of H material show quartz as the dominating, load bearing, and cementing mineral. The cementation is extensive, and calcite as well as feldspar minerals, also

detected by XRD, are embedded as single crystals in the solid frame. Phyllosilicates appear in the pore space (Figure 2.1d).

BSEM-images of C material show quartz as the dominating mineral and load bearing, but with a significant quantity of feldspar and bands of phyllosilicate-bearing stylolites. Compared to O and H the cementation is relatively low (Figure 2.1e and f).

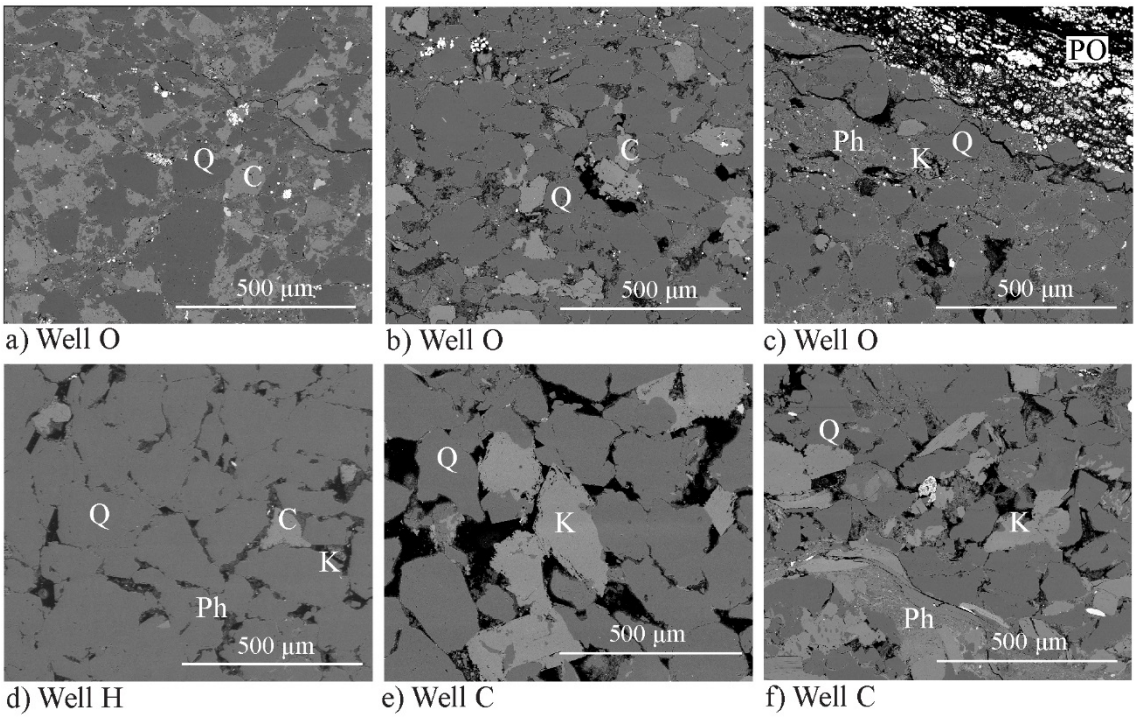

Figure 2.1 BSEM-images of sandstone from well O, H and C, representing side-trim material from plugs. Q = quartz, C = calcite, K = feldspar, Ph = phyllosilicate, P = pyrite, PO = pyrite in organic matter.

The measured range of grain density of 2.73-2.85 g/cm^3 for O specimens corresponds to the presence of calcite and pyrite found by XRD and EDS analysis. Nitrogen porosity (ϕ_N) ranges from 0.05 to 0.12 and Klinkenberg corrected gas permeability (k_K) is in general below 0.015 mD. Caused by the presence of highly porous organic matter, the relatively high specific surface from Nitrogen absorption (BET) of 6.5 m^2/g (Table 2.2) does not represent the specific surface of the minerals. The carbonate content of O material ranges from 5 % to 37 % (Table 2.2). The significant range in characteristics for samples from well O, suggests great caution in direct comparison across individual samples.

A measured grain density of 2.64 g/cm^3 for H specimens corresponds to the dominance of quartz minerals found by XRD and EDS analysis. Measured nitrogen porosity and Klinkenberg corrected gas permeability are around 0.12 and 0.12 mD respectively. The specific surface from BET is 0.9 m^2/g as expected for a quartz dominated sandstone with pore-filling phyllosilicates and the carbonate content range is tight around 3% (Table 2.2).

A measured grain density of 2.67 g/cm^3 for C specimens corresponds well with findings from XRD analysis and the dominance of quartz in addition to a significant presence of the slightly heavier phyllosilicates. Measured nitrogen porosity is around 0.2, and Klinkenberg corrected gas permeability ranges from 0.3 to 105 mD, probably related to the extent and number of tight phyllosilicate stylolites. The specific surface by BET is 1.7 m^2/g corresponds to a sandstone with a significant presence of phyllosilicates. The carbonate content is low in accordance with results from XRD and EDS.

Table 2.2. Range of measured properties of reservoir sandstone samples.

Well	Dry density, ρ_d	Grain density, ρ_m	N_2 Porosity, ϕ_N	Klink. corr. Permeability, k_K	Specific surface, BET	Carbonate content
	g/cm^3	g/cm^3	-	mD	m^2/g	%
O	2.39 - 2.56	2.73 - 2.85	0.03 - 0.14	<0.01 - 0.123	6.5	5 - 37
H	2.30 - 2.38	2.63 - 2.64	0.11 - 0.13	0.11 - 0.22	0.9	1.1 - 4.2
C	2.01 - 2.22	2.66 - 2.68	0.19 - 0.20	1.78 - 104.62	1.7	0.6 - 1.7

2.2 Outcrop sandstones

The outcrop sandstone material experimentally investigated in studies of thermal conductivity and permeability originate from 1) Fontainebleau, France, 2) Castlegate, USA, 3) Bentheim, Germany, 4) Obernkirchen, Germany and 5) Berea, USA. In studies of thermal conductivity and permeability respectively 19 and 13 samples were used.

From semi-quantitative XRD analysis, quartz is the dominating mineral in all the studied outcrop sandstones (Table 2.3). From XRD analysis feldspar is detected in samples from Castlegate and Bentheim and phyllosilicates in Castlegate, Obernkirchen, and Berea samples. BSEM-images confirm quartz as the dominating, but also as the load bearing mineral and cementing mineral. The cementation degree however varies between sampling locations. With the exception of Fontainebleau sandstone phyllosilicates are

seen in all samples (Figure 2.2). Some Fontainebleau samples show weak grain contacts, presumably related to weathering. Bentheimer samples show no presence of phyllosilicates from XRD, but from BSEM clusters of kaolinite are detected (Figure 2.2c). Thus, in accordance with Peksa et al., (2017) a clay content of 2.7 % is listed for Bentheimer sandstone in Table 2.3.

Table 2.3. Mineralogical composition of outcrop material as detected by EDS and semi-quantitative XRD.

Formation	Quartz	Kali-feldspar	Phyllosilicate
	mass % of total solid		
Fontainebleau	100		
Castlegate	95.4	1.1	3.5
Bentheimer	95.3	4.7	(2.7)[a]
Obernkirchen	96.0		4.0
Berea	95.0		5.0

[a](Peksa et al., 2017)

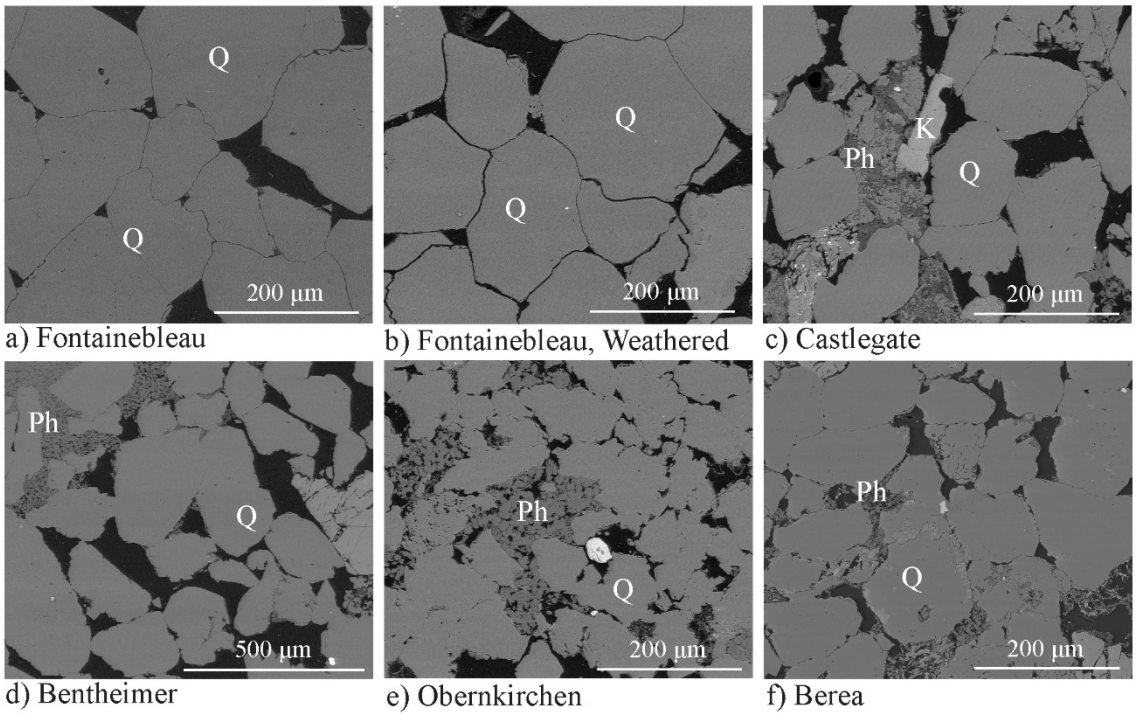

Figure 2.2 BSEM-images of sandstone from well O, H and C, representing side-trim material from plugs. Q = quartz, C = calcite, K = feldspar, Ph = phyllosilicate, P = pyrite, PO = pyrite in organic matter.

Grain density close to 2.66 g/cm^3 (Table 2.4) corresponds to the dominance of quartz in all samples. Nitrogen porosity ranges from 0.05 to 0.28 and permeability from 0.6 to 430 mD and thus wide ranges are investigated. High measured specific surface by BET (Table 2.4) corresponds to samples with presence of phyllosilicates as detected from XRD and BSEM (Table 2.3 and Figure 2.2).

Table 2.4. Range in measured properties of outcrop sandstone samples.

Formation	Dry density, ρ_d	Grain density, ρ_m	N_2 Porosity, ϕ_N	Permeability		Specific surface, BET
				Klink.[a] k_K	Water, k_w	
	g/cm^3	g/cm^3	-	mD		m^2/g
Fontainebleau	2.32 - 2.53	2.65 - 2.66	0.047 - 0.234	0.3 - 140	0.3 – 430	0.03
Castlegate	1.91 - 1.92	2.67	0.279 - 0.284	290 - 320	260 – 350	1.72
Bentheimer	1.97 - 1.98	2.66 - 2.68	0.262 - 0.265	-	320	0.31
Obernkirchen	2.15 - 2.21	2.67	0.175 - 0.196	4.5 - 7.3	1.5 - 3.5	1.06
Berea	2.17 - 2.20	2.68	0.186 - 0.193	10 - 50	-	1.50

[a]Klinkenberg corrected gas permeability

3. TEMPERATURE EFFECTS ON THE EFFECTIVE STRESS

3.1 The concept of effective stress

Originally introduced by Terzaghi in the 1920s, the concept of effective stress brought a theoretical formulation of the relation between total stress, pore pressure and the strain (effective stress) in a soil volume undergoing deformation. In the classical paper "*General theory for three-dimensional consolidation*", Biot (1941) formulated a generalized elastic theory, where he introduced the coefficient, α, now denoted as Biot's coefficient or the effective stress coefficient. For isotropic stress and isothermal conditions, Biot's equation may be formulated as:

$$\sigma_{\text{eff}} = \sigma_{\text{tot}} - \alpha P, \tag{3.1}$$

where σ_{tot} is the total stress, P is the fluid pore pressure and σ_{eff} is the effective stress. Biot's coefficient and P are scalars, whereas σ_{tot} and σ_{eff} in principle are 3 by 3 tensors, but simplified and treated as scalars in the isotropic case because of stress symmetry. Equation 3.1 shows that the pore pressure is counteracting the total stress and defining the effective stress as reflected in the resulting deformation. Biot's coefficient can by definition only obtain values between porosity and 1, and in the case of sedimentary rocks Biot's coefficient is less than 1 ($\alpha < 1$), and consequently only a fraction of the pore pressure (αP) in sedimentary rocks counteracts the total stress (equation 3.1). Biot's coefficient is defined as:

$$\alpha = 1 - K_{\text{dra}} / K_{\text{min}} \tag{3.2}$$

where K_{min} is mineral bulk modulus, and K_{dra} is the drained bulk modulus, i.e., the frame bulk modulus, K_{frame}. The term modulus defines a measure of elastic stiffness and is hence a quantification of the resistance of a material to elastic deformation resulting from an applied stress. K_{dra} is typically determined from compressional and shear moduli of rocks in the dry state as $K_{\text{frame}} = K_{\text{dry}} = M_{\text{dry}} - 4/3G_{\text{dry}}$ where $M_{\text{dry}} = \rho V_{\text{P,dry}}^2$ and $G_{\text{dry}} = \rho V_{\text{S,dry}}^2$ are compressional and shear moduli and ρ_{dry}, $V_{\text{P,dry}}$ and $V_{\text{S,dry}}$ are dry density, dry compressional and dry shear wave velocities, respectively.

3.1.1 Estimating the grain contact area from Biot's coefficient

The frame stiffness of sedimentary rocks consisting of single grains cemented together to constitute a solid and porous frame is controlled by the degree of cementation as well as the stiffness (modulus) of constituting grains. It is measured under fully drained conditions. Stress and strain are by convention considered positive for respectively compression and compaction. The corresponding volumetric elastic strain, ε_b, resulting from changes in σ_{tot} and P in equation 3.1 can be expressed in a constitutive relation as:

$$\varepsilon_b = K_{dra}^{-1}(\sigma_{tot} - \alpha P), \tag{3.3}$$

which equate

$$\varepsilon_b = \varepsilon_{tot} + \varepsilon_P, \quad \varepsilon_P = -\alpha P K_{dra}^{-1}, \tag{3.4}$$

where ε_{tot} is the volumetric strain from changes in the total stress, and in accordance with equation 3.1, ε_{tot} is in principle a tensor, but treated as a scalar in the present case. ε_P is the volumetric strain from changes in pore pressure. The resulting elastic compaction, ε_b, for α less than one ($\alpha < 1$) is smaller than for $\alpha = 1$, as only the reduced pore pressure (αP) counteract the total stress (equation 3.3 and 3.4). Because the pore pressure requires access to the pore walls to counteract the total stress, α conceptually represents the area with countering pore pressure and consequently the residual $(1 - \alpha)$ must represent the inaccessible cemented area, leading to the conceptual interpretation that the cemented contact area is equal to $(1 - \alpha)$. The concept of effective stress can thus relate Biot's coefficient to the grain contact area (cemented area) as discussed by Gommesen et al. (2007), Alam et al. (2009), and Fabricius (2010). Fabricius (2010) illustrated the concept as in Figure 3.1 and show that knowledge of Biot's coefficient conceptually provides a quantitative measure of the grain to grain contact area.

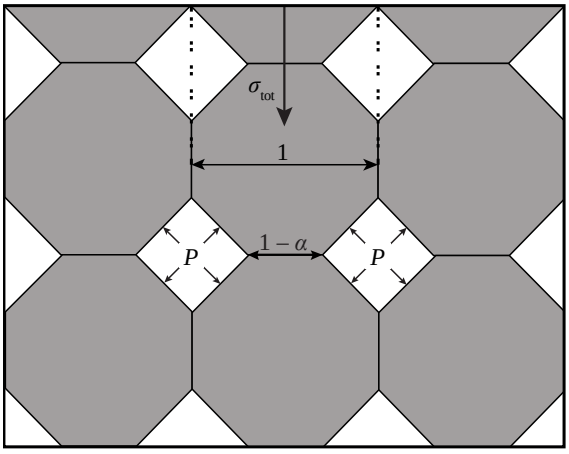

Figure 3.1. Conceptual sketch of a porous sedimentary rock with saturating fluid (white) and sediment particles (gray) connected by contact cement (after Fabricius, 2010) illustrating $(1 - \alpha)$ as quantification of the cemented area (grain to grain contact).

3.2 The non-isothermal effective stress in sedimentary rocks

Biot assumed isothermal conditions in his original formulation, as represented by the effective stress (equation 3.1), but Palciauskas and Domenico (1982) and McTigue (1986) later formulated the non-isothermal equivalent by combining poro- and thermoelastic theory. Defining compaction from poroelastic effects and contraction from thermoelastic effects as positive strain, the resulting non-isothermal volumetric strain $\varepsilon_{b,T}$ for isotropic stress can be expressed as:

$$\varepsilon_{b,T} = \varepsilon_{tot} + \varepsilon_P + \varepsilon_T, \quad \varepsilon_P = -\alpha P K_{dra}^{-1}, \quad \varepsilon_T = -\beta T, \tag{3.5}$$

where $\varepsilon_{tot} + \varepsilon_P$ is the isothermal strain from equation 3.4, ε_T is the thermoelastic strain due to a temperature change, T, and β is the volumetric thermal expansion coefficient of the constituting mineral.

Conversion between strain and stress in porous rocks is not straightforward for non-isothermal conditions, because depending on the boundary condition, temperature increase is physically linked to changes in pore pressure. For a fluid saturated porous rock one can imagine two conditions where increased temperature are coupled respectively uncoupled with increase in pore pressure: 1) at undrained conditions and zero volume change, the difference in expansion of the fluid and solid constituents will lead to the necessity of a coupling term when increased temperature induce pore pressure increase;

2) at drained condition with a constant pore pressure, temperature increase induces changes only on the solid frame. This can be the case, where increased load on a water column simultaneously with a temperature increase lead to zero change in fluid density. Then pore pressure and temperature effects are uncoupled.

Thermal strain, induced on the solid frame from increased temperature with pore pressure uncoupled from temperature increase, can physically only convert to stress when the boundary conditions are that of a rigid constraint. A rigid constraint implies that for a representative volume, the thermally induced volume change is zero, and as an equivalent to equation 3.5, the non-isothermal stress can under this condition be formulated as:

$$\sigma_{\mathrm{eff},T} = \sigma_{\mathrm{tot}} + \sigma_{\mathrm{P}} + \sigma_T,\ \sigma_P = -\alpha P,\ \ \sigma_T = -\beta T K_{\mathrm{dra}}, \tag{3.6}$$

where σ_P and σ_T are respectively the poro- and thermo-elastic stress.

Equation 3.5 shows that strains from both pore pressure and temperature are counteracting $\varepsilon_{\mathrm{tot}}$ and consequently also σ_{tot} (equation 3.6) when conditions leading to the conversion of thermal strain to stress are present. Thus, in a representative volume, the counteracting poro- and thermoelastic volumetric strains (ε_P and ε_T), resulting from change in P and T may lead to negative $\varepsilon_{\mathrm{b},T}$ (equation 3.5). However, only the surplus strain (the portion of $\varepsilon_{\mathrm{b},T}$ leading to apparent $\varepsilon_{\mathrm{b},T} < 0$) can result in an overall volumetric expansion. Consequently the remaining $\varepsilon_{\mathrm{b},T}$ leading to $\varepsilon_{\mathrm{b},T} > 0$ is converted to thermal stress when the total stress exceeds or is equal to the counteracting stress from pore pressure and temperature. With respect to thermal strain-stress conversion, the boundary condition of equation 3.6 is then:

$$\sigma_T \neq 0 \Leftrightarrow \sigma_{\mathrm{tot}} \geq \left|\sigma_P + \sigma_T\right|, \tag{3.7}$$

and by stating conditions of $\sigma_{\mathrm{eff},T} \geq 0$ at all times, equation 3.6 becomes:

$$\begin{aligned} &\sigma_T \neq 0 \Leftrightarrow \sigma_{\mathrm{tot}} \geq \left|\sigma_P + \sigma_T\right|,\ \sigma_{\mathit{eff},T} \geq 0, \\ &\sigma_{\mathrm{eff},T} = \sigma_{\mathrm{tot}} + \sigma_{\mathrm{P}} + \sigma_T,\ \sigma_P = -\alpha P,\ \ \sigma_T = -\beta T K_{\mathrm{dra}}. \end{aligned} \tag{3.8}$$

Thus, when the total stress exceeds the counteracting from pore pressure and temperature, a representative rock volume is rigidly constrained, and conversion of thermal strain to stress can follow.

Table 3.1. Bulk modulus and the thermal expansion coefficient of common minerals.

Mineral	Bulk Modulus, K_{min}, (GPa)	Linear thermal expansion coeff., η, (10^{-6} K^{-1})	Volumetric thermal expansion coeff., β, (10^{-6} K^{-1})
Quartz	37[a]	7.7[b,1], 13.5 [b,2]	34.7[c]
Calcite	72[a]	–4.4[b,1], 23[b,2]	14.6[c]
Feldspar	75.6[a]	1.3[b,3], 13.5 [b,4]	19.8[c]
Clay/shale	25[a]		31[d]

[a]Citation in Mavko et al. (2009), [b]Johnson and Parsons (1944), [c]Derived as the sum of linear thermal expansion coeff., [d]Estimate based on work by McKinstry (1965), [1]Parallel to c-axis, [2]Perpendicular to c-axis, [3]Parallel to b-axis, [4]Parallel to a-axis.

By examining the non-isothermal effective stress, with respect to a representative volume in the subsurface, formation (e.g., σ_{tot}, P and T) and material properties (e.g., K_{dra}, K_{min} and β) simultaneously control the resulting magnitude of $\sigma_{eff,T}$ as well as the pre-condition for a strain to stress conversion (equation 3.8). However, it might not be the magnitude, but the respective ratios of K_{min} and β that are controlling $\sigma_{eff,T}$ because changes in pore pressure and temperature with depth are not necessarily equally proportional. For instance, depth correlation of subsurface temperature is as a first approximation linearly to great depth, whereas the pore pressure is typically not, because of overpressured formations. For a quartz dominated sandstone with respectively K_{min} and β of 37 GPa and $34.7 \cdot 10^{-6}$ K^{-1} (Table 3.1) the ratio between K_{min} and β approximate 10^6 GPa/K whereas for a calcite dominated limestone with K_{min} and β of respectively 72 GPa and $14.6 \cdot 10^{-6}$ K^{-1}, the ratio approximates $5 \cdot 10^6$ GPa/K (Table 3.1). There is thus a factor 5 difference between quartz and calcite and by imagining the two rocks at equal depth (equal σ_{tot}) and assuming equal frame stiffness (K_{dra}) the resulting $\sigma_{eff,T}$ must be different, because of the different ratio.

3.3 Case study: the non-isothermal stress of the Hejre Field, North Sea

By using data from the Danish oil field Hejre situated in the North Sea (Figure 3.2), it is possible to evaluate possible consequences of including non-isothermal conditions in estimation of the subsurface effective stress.

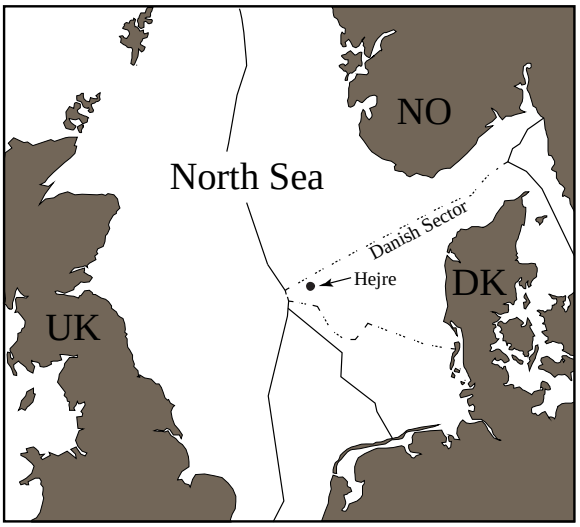

Figure 3.2. Map of the central North Sea.

Data from the Hejre field goes as deep as 5.4 km, and by using downhole measurements, Regel et al. (2017) estimated frame stiffness, Biot's coefficient, overburden stress, temperature and the range of pore pressure in the depth interval from 3000 to 5400 meters depth (Figure 3.3).

By assuming a salinity of 90,000 ppm and by inserting pore pressure and temperature data from Figure 3.3b in the expression for brine density by Batzle and Wang (1992) one finds a density decrease in the order of 5%. The volume expansion from increased temperature is thus slightly higher than the volume decrease from compression. If assuming that this effect is negligible, each term in equation 3.8 becomes uncoupled. Further, if assuming isotropic stress symmetry and coefficients of thermal expansion from Table 3.1 corresponding to each lithology shown in Figure 3.3a, the range of non-isothermal effective stress ($\sigma_{\mathrm{eff},T}$) can be calculated from equation 3.8 as a function of depth (Figure 3.3b). For comparison, in one case the isothermal effective stress, σ_{eff}, was derived from Biot's original formulation, and in one case from Terzaghi's concept by assuming $\alpha = 1$ ($\sigma_{\mathrm{eff},\alpha=1}$), which is common in geotechnics.

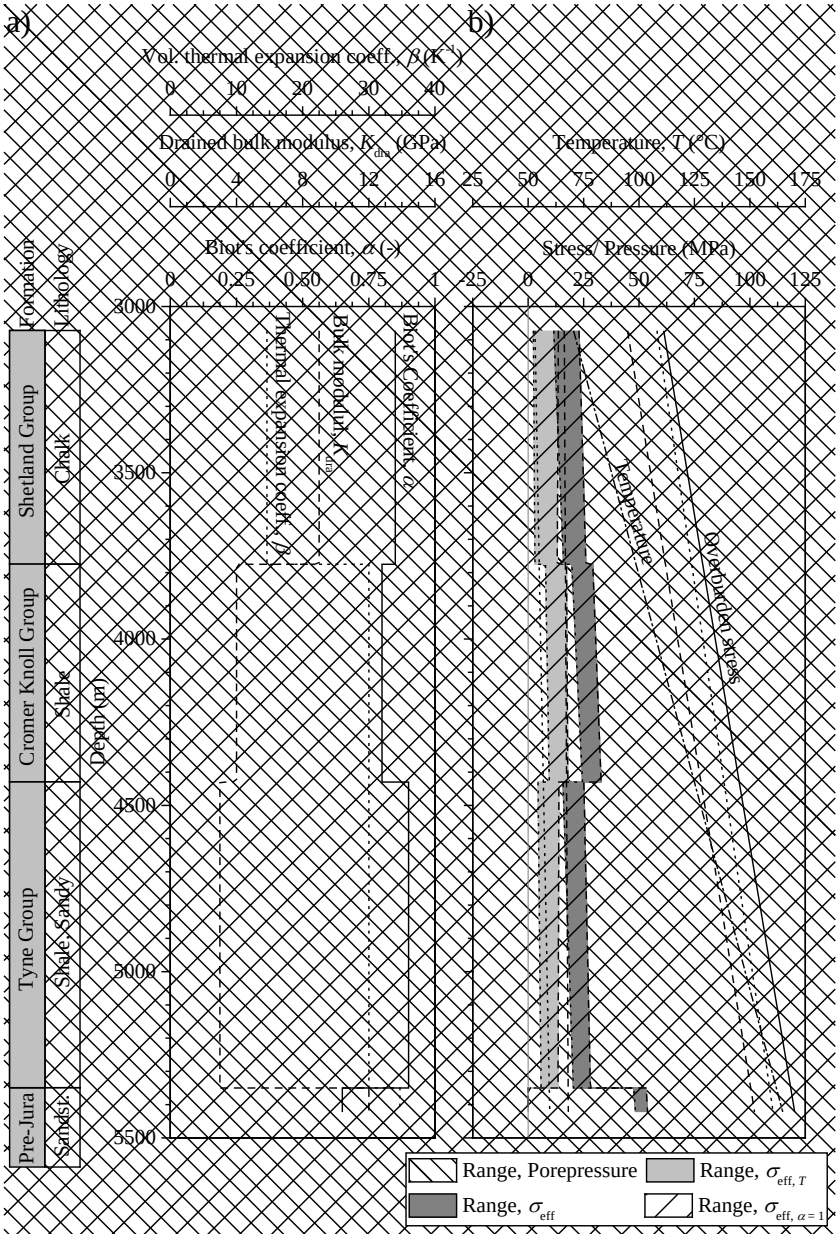

Figure 3.3. North Sea case study. a) Estimates of temperature, drained bulk modulus and Biot's coefficient as function of depth for the Hejre field. Estimates are from Regel et al. (2017). The coefficient of thermal expansion is estimated based of the respective lithology for each formation and Table 3.1. b) Calculated range of effective stress as function of depth. The overburden stress and pore pressure range is from Regel et al. (2017).

In the studied lithological sequence, the derived $\sigma_{\text{eff},T}$ is practically constant with depth and closely approximates $\sigma_{\text{eff},\alpha=1}$ in the chalk and shale formations (Shetland, Cromer Knoll, and Tyne Groups) (Figure 3.2b). Approximating Biot's coefficient equal to one,

leads to the assumption of $\sigma_{eff,\alpha=1} = \sigma_{eff}$, which is typically used in planning of well drilling, and in the investigated depth range, the assumption is most likely wrong but appear as a successful choice for estimation of the effective stress (Figure 3.2b).

The pre-condition of equation 3.8 is violated in the Pre-Jura section showing that the thermal strain (ε_T) is only partly converted to stress so that the surplus strain presumably resulted in an expansion of the formation. Jointly, results from the case study indicate that sections or entire formations in the subsurface of the deep North Sea basin are experiencing neutral effective stress. Hence, overlying layers are in principle floating on overpressured layers below and because of the low stiffness to thermal expansion ratio of quartz (Table 3.1), the threshold is presumably located at depths where Triassic or Jurassic sandstones are found.

4. TEMPERATURE EFFECTS ON STIFFNESS AND STRENGTH PROPERTIES OF SANDSTONES

Sampling of subsurface material inevitably involves equilibration of material to atmospheric conditions and in literature the equilibration is speculated to induce tensional forces in the grain contacts, leading to ruptures of the weakest contact cement (Holt 1994). The ruptured contacts cause a reduction in stiffness and are in the rock physical society denoted as micro-cracks posing a single bulk term. The term is, however, unfortunate for several reasons: 1) ruptures due to stress release and due to cooling are different in both physical principle and presumably in order of magnitude; and 2) ruptures originating from cooling must be considered homogeneously distributed but related to the mineralogical composition, whereas ruptures from stress release are not necessarily so, because of possible anisotropy in the subsurface stress field. Both outcrop and reservoir material were buried in the geological past before being brought to the surface and consequently micro-cracks are found in both material types. The timescale of equilibration to atmospheric conditions are however different in the two cases, but not the physical mechanisms resulting in micro-cracks. One important physical consequence of micro-cracks is that sampled rock material cannot fully represent in-situ material because reestablishment of stress and temperature in the laboratory will not heal ruptured contacts.

4.1 Temperature effect on rock stiffness

By reestablishing in-situ stress and pore pressure conditions, several studies have shown increased frame stiffness for various lithologies, and the stiffening has been related to reestablishment of ruptured grain contacts (e.g. Banthia et al., 1965; Nur and Simmons, 1969; Wu et al., 1991; Frempong et al., 2007 and Mavko and Vanorio, 2010). Denoting the effect as micro-crack closure, frame stiffening from stress is thus well documented and accepted in the geo-mechanical society. On the other hand, limited studies on rock stiffness at elevated temperature, including controlling mechanisms results in an incomplete picture of effects from temperature. Further, studies on stiffness properties as a function of temperature are generally written in context for three applications: 1) petroleum and geothermal industries, 2) nuclear waste deposits and 3) fire damage on buildings and monuments. Experimental studies with application in the petroleum and geothermal industries, as well as in nuclear waste deposits, generally concern temperatures below 300°C (e.g. Hughes and Cross, 1951; Hughes and Kelly, 1952;

Handin and Hager, 1958; Mobarak and Somerton, 1971; Timur, 1977; Rao et al., 2007; Hassanzadegan et al., 2011) whereas studies related to fire damage and to some degree, nuclear waste deposits include temperatures as high as 1200°C (e.g., Hajpál, 2002; Mao et al., 2009; Ranjith et al., 2012; Zhang et al., 2009 and Wu et al., 2013). The difference in context and application of experimental results is presumably directly correlated to the scatter in lithology, maximum testing temperature, and saturating pore fluids found in the literature. Independent of application, commonly stiffness properties are evaluated with reference to ambient temperature presumably because it is straightforward from an experimental and practical point of view. However, from a physical point of view, ambient temperature is as foreign to the material as temperatures above in-situ. Theories and properties derived from experimental data on both downhole sampled and outcrop material, consequently need evaluation with the material's geological temperature history in mind. Such studies are limited, but include a publication by Timur (1977), stating temperature history as a factor affecting ultrasonic velocities is rocks. By contrast, addressing pre-consolidation as well as in-situ stress level and symmetry through the materials geological stress history is fully implemented in geo-mechanical societies.

Material sampled from downhole are commonly limited in quantity, and consequently, outcrop materials are often used as an analog. However, failure to envisage differences in temperature history between downhole and outcrop material may give rise to difficulty when assessing temperature effects on, e.g., stiffness properties. This would suggest the use of analog material selected by equally envisaging the geological temperature history (i.e., maximum in-situ temperature) in addition to more conventional parameters (e.g., porosity, permeability, and mineralogy). Failure to envisage the geological temperature history in principle makes conclusions on, e.g., rock stiffness from temperature controlled experiments unique to the studied material; leaving high chance of finding a misguided use of analog materials. This again may lead to an unreasonable use of temperature trends in an evaluation of in-situ reservoir properties such as stiffness.

Compared to ambient conditions, at experimentally reestablished in-situ temperature, a studied rock frame may either stiffen, soften or behave neutrally. However, the constituting mineral stiffness may behave differently to temperature than the frame stiffness. For example, the constituting quartz minerals in sandstones will experience a softening trend for increasing temperature (Orlander et al., I) whereas closure of micro-

cracks by thermal expansion of the minerals following from the temperature increase should stiffen the frame. Similarly, if the boundary conditions are that of a rigid constraint and constant pore pressure, thermal expansion of constituting mineral reduces the resulting strain ($\varepsilon_{b,T}$) and the material thus behaves stiffer (equation 3.5). Hence, with respect to properties of the constituting mineral, the overall change in frame stiffness for reestablished in-situ temperature, are simultaneously controlled by the magnitude of stiffness versus temperature trends and the thermal expansion coefficient. The latter can induce potential stiffening by two different mechanisms described as:

- Mechanism 1: consider a rock sample with a constantly applied total stress and pore pressure and with effective stress below the stress leading to full micro-crack closure. Restitution of temperature to previous equilibrium causes closure of contact cement ruptures (i.e., of micro-cracks) by thermal expansion of the constituting rock minerals, hence leading to stiffening of the rock frame. Because a rock volume is assumed homogeneous and un-fractured in the constitutive formulations in equation 3.8, it is incapable of describing this mechanism. Further, at a constant temperature, an increase in applied stress may enlarge the contact area in ruptures possibly created by thermal shrinkage, and continued stress increase will add to the number of contacts or increased contact area of existing contacts, thereby leading to stiffening.
- Mechanism 2: consider the same rock sample, but with constantly applied total stress and pore pressure equivalent to full micro-crack closure and with the resulting strain ε_b in accordance with equation 3.3. Restitution of in-situ temperature will inevitably cause thermal expansion of the rock minerals, and the resulting strain may be in accordance with equation 3.5 and equal to $\varepsilon_{b,T}$, if applied stress and pore pressure respect the boundary conditions of rigidly constrained volume/rocks frame ($\sigma_{eff,T} > 0$). Assuming this is so, the rock frame might behave stiffer at in-situ temperature, depending on the proportion of the material petrophysical properties (K_{min} and β). Physically, the stiffening can be caused by the conversion of the thermally induced strain to thermal stresses internally imposed on the rock frame. Thus, stiffening of the rock frame from thermal stress occurs only when $\sigma_{eff,T} > 0$ and is maximum when $\sigma_{eff,T} = 0$.

4.2 Temperature effects on rock stiffness - experimental results

Experimental results of dry rock stiffness derived at different boundary conditions, and temperatures from ambient to in-situ on downhole sampled material from well O, H and C (section 2.1), compose the background for the arguments of Mechanisms 1 and 2 respectively. As testing was done on samples in the dry state experiments are in principle drained.

4.2.1 Mechanisms 1 – closure of micro-cracks from thermal expansion

To determine if the grain contact area, acknowledged as $(1 - \alpha)$ (section 3.1), increases because of micro-crack closure by thermal expansion (Mechanism 1), the stiffness of investigated sample materials was measured in a stress regime with partially closed micro-cracks and thermally unconstrained sample volume (See Orlander et al. I for argument on constrained sample volume).

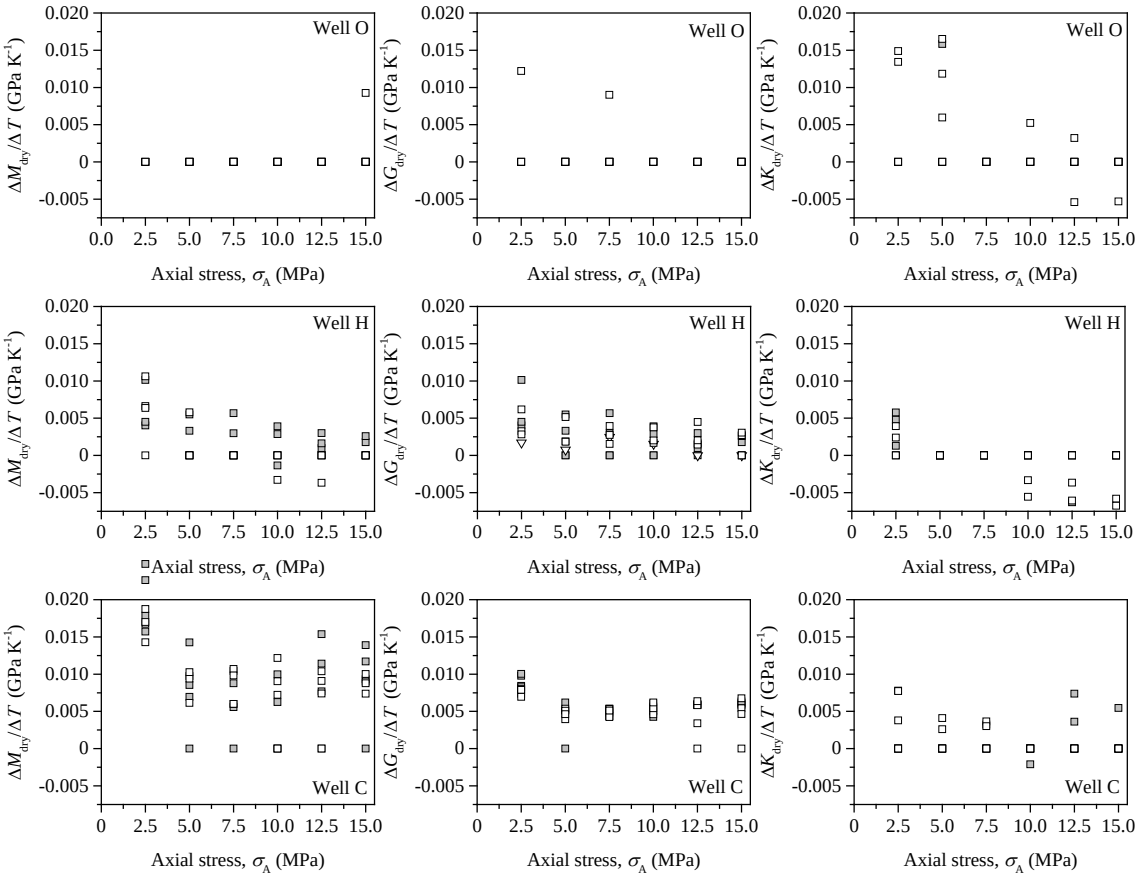

Figure 4.1. Changes in elastic moduli, M_{dry}, G_{dry} and K_{dry} for change in temperature versus axial stress level. Data are from Orlander et al., I. Gray marked represent hydrostatic stress symmetry and white constant confining of 2 MPa. Slopes of modulus versus temperature not significantly different from zero as determined from ANOVA analysis are plotted as zero.

At axial stress from 2.5 to 15 MPa and temperatures of ambient, 50°C 100°C 150°C and in-situ (170°C), dry elastic moduli of compression (M_{dry}) as well as shear (G_{dry}) derived from dry density and ultrasonic velocities show a slight increase in modulus for increased stress and with the exception of O material also a slight increase for increased temperature (Orlander et al. I). Deriving K_{dry} from M_{dry} and G_{dry} (section 3.1) and subsequently calculating slopes of M_{dry}, G_{dry}, and K_{dry} versus temperature, accounting for slopes not significantly different from zero, show O material unaffected by temperature. However, for H and C material the temperature affected M_{dry} and G_{dry} are counteracting, resulting in K_{dry} generally unaffected by temperature (Figure 4.1). By using a temperature corrected quartz modulus, K_{min} of:

$$K_{min} = -3.2 \cdot 10^{-5} T^2 - 4.1 \cdot 10^{-3} T + 38.1 \qquad (4.1)$$

where T is the temperature in °C and K_{min} is in GPa (Orlander et al. I). Biot's coefficient derived from K_{dry} in general show none to minor temperature dependency (Figure 4.2), signifying closure of ruptured grain contacts by thermal expansion as minor in the investigated stress and temperature regime. Consequently, compared to micro-cracks closure by increased stress level the observed thermal stiffening is insignificant.

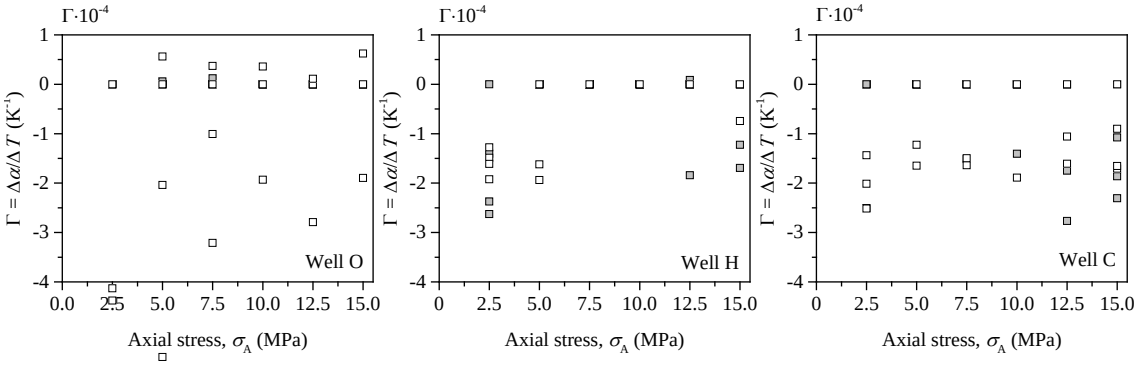

Figure 4.2. Change in Biot's coefficient with change in temperature versus axial stress level for sandstone samples. Data are from Orlander et al., I. Gray marked represent hydrostatic stress symmetry and white constant confining of 2 MPa.

Recalling that results are obtained from volumetrically unconstrained samples, one could imagine a larger stiffening effect from thermal micro-crack closure in condition with a constrained sample volume. However, the present data do not include boundary

conditions where stress levels correspond to a constrained sample volume and where micro-cracks are not closed by the stress. Hence, the present data do not provide the full picture of micro-crack closure by thermal expansion of constituting minerals.

4.2.2 Mechanisms 2 – stiffening from an increase in internal stress

To determine if thermally induced internal stress in the rock frame can lead to stiffening (Mechanism 2) the rock stiffness of investigated samples was measured in a stress regime with full micro-cracks closure and thermally constrained sample volume (See Orlander et al. I for argument on constrained sample volume). Two samples were at identical confining stress, but at either ambient or in-situ temperature brought to failure by increasing axial stress and the static *E*-modulus was derived from stress-strain curves (Figure 4.3). From continuously, measured ultrasonic velocities and deformation corrected density the dynamic *E*-modulus, E_{dyn}, was derived.

Static *E*-modulus of O specimens show an incomplete picture of temperature effects because stiffening and softening changes for different confining stress (Figure 4.3) and discrepancies in stiffening and softening trends are found from dynamic *E*-modulus, adding further to the incomplete picture for O material (Figure 4.3). Significant heterogeneity on the sample scale (Chapter 2) is probably making comparison across samples unreasonable. On the other hand, the high degree of homogeneity found in H and C specimens (Chapter 2) makes direct comparison of temperature effects on the rock stiffness at high stress levels possible and for H as well as C material both E_{sta} and E_{dyn} are higher at in-situ temperature (Figure 4.2) when the confining stress is above 3 MPa. The higher stiffness at in-situ temperature is interpreted as thermal strain converted to increased internal stress thus increasing the stiffness as suggested in mechanism 2.

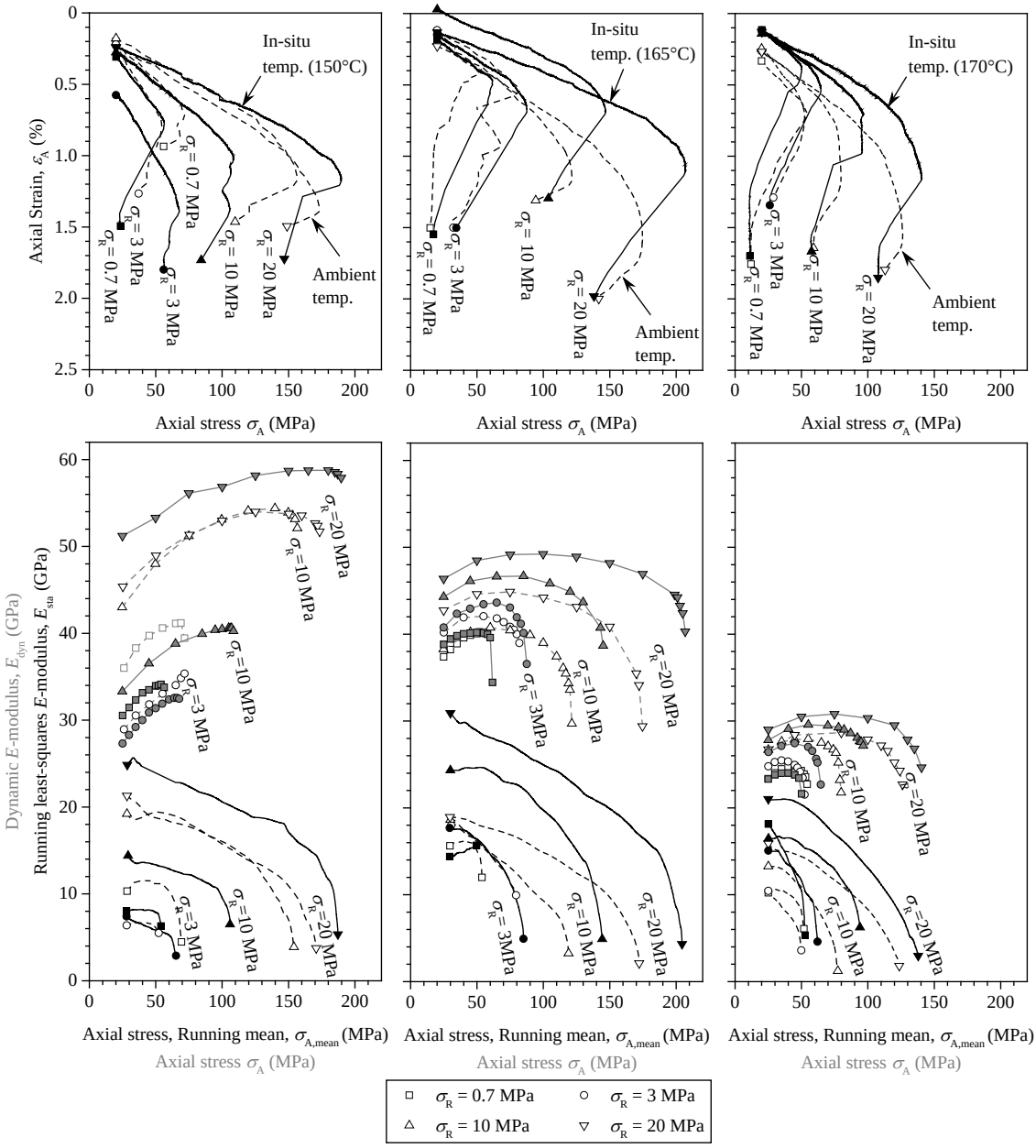

Figure 4.3. 1st row) Stress-strain curves at ambient and in-situ temperature. 2nd row) Axial stress versus, static and dynamic *E*-moduli. E_{sta} is derived from stress-strain curves using a running least squares best fit with a length of 5 MPa. Data are from Orlander et al., I.

4.3 Temperature effect on rock strength - experimental results

Arguments made in section 4.1, on the common lack of considerations to the materials' geological temperature history, with respect to temperature effects on the frame stiffness, are similar with respect to rock strength, and thus also the difficulties arising with

misguided use of analog material and contradictory conclusions from experimental results.

A material's shear strength is in classical rock mechanics commonly, described from Mohr-Coulomb's failure criteria by the material's effective stress friction angle (φ') and cohesion (c') (Jaeger et al., 2007). φ' describes the material's frictional shear resistance and, c' the bonding between grain contacts (cohesion). The shear strength of rock material is commonly derived from a series of triaxial failure tests and a critical state (failure criteria) defined from the measured peak stresses in the p' - q work frame, where p' is the mean effective stress and q is the deviatoric stress, defined as:

$$\begin{aligned} p' &= \frac{1}{3}(\sigma_1' + \sigma_2' + \sigma_3') \\ q &= \sqrt{\frac{(\sigma_1' - \sigma_2')^2 + (\sigma_2' - \sigma_3')^2 + (\sigma_1' - \sigma_3')^2}{2}}, \end{aligned} \tag{4.2}$$

where σ'_1, σ'_2, and σ'_3 are the normal stresses and the standard notation is that σ'_1 is the axial stress, whereas σ'_2 and σ'_3 are the radial.

Temperature-induced stiffening of the rock frame was in the previous section related to the thermal expansion of the constituting minerals and for temperature induced strengthening similar arguments can likewise be related to thermal expansion. For most sedimentary rocks, conditions leading to shear failure follow stress levels of full micro-crack closure and strengthening by a thermally induced closure of micro-cracks is thus unfeasible. However, a thermal stress induced by thermal expansion of constituting minerals can lead to strengthening. Consider a rock volume exposed to thermal strains due to a temperature increase, and assume conditions leading to the conversion of thermal strain to stress (section 3.2). The thermal stress (σ_T) will thus induce internal stresses, consequently leading to increased frictional forces in the grain contacts, and result in increased shear resistance and friction angle. On the other hand, as frictional forces do not induce changes to the physical bonding of the grain contacts, the cohesion is unaffected by changes in internal stress, when assuming that the cementing minerals have only negligible strength variation with temperature.

The mean effective stress p' and the deviatoric stress q, derived from the axial peak stress as well as the confining stress of the conducted experimental work, gives an incomplete

picture of temperature effect for O-material, and as for the stiffness (section 4.2), discrepancies in petrophysical characteristics are presumably the cause. *p´* - *q* diagrams of peak (failure) stresses of H as well as C material, show increased strength at in-situ temperature (Figure 4.4), and the material's friction angle (*φ´*) is approximately 4 degrees higher. On the other hand, the cohesion is practically unaffected by temperature. As the stress conditions leading to mechanical failure in the conducted testing allow for conversion of thermal strain to stress, the increased shear resistance (friction angle) observed from ambient to in-situ temperature is a direct consequence of increased frictional forces in the grain contacts resulting from increased internal stress.

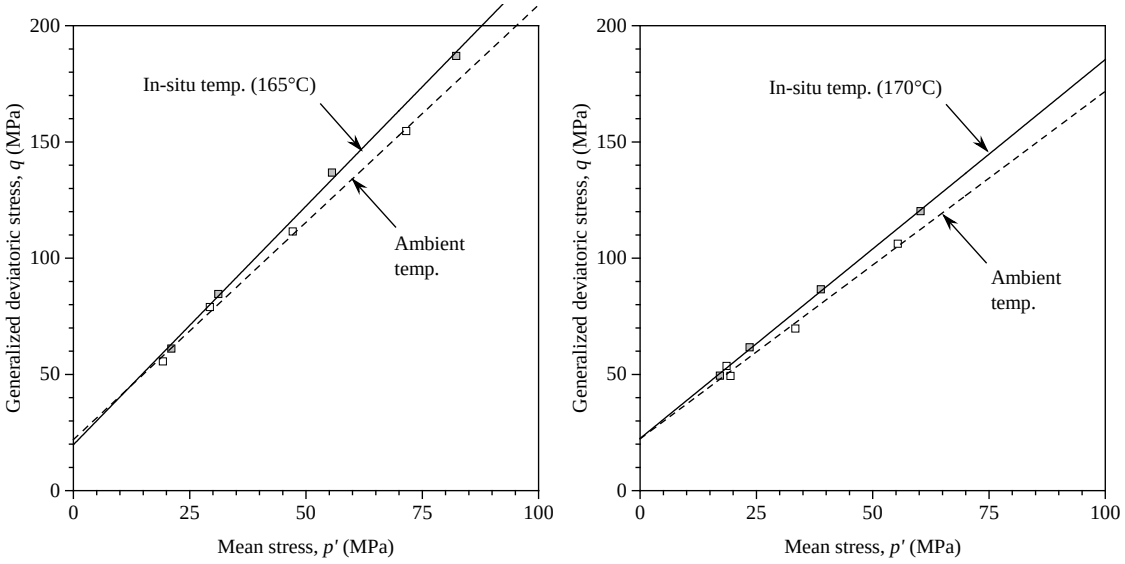

Figure 4.4 *p´* - *q* diagrams of dry H and C material at ambient and in-situ temperature. Data are from Orlander et al., 2018b.

5. PERMEABILITY OF SANDSTONES - CONTROLLING PORE SIZE

From the classical Darcy definition, permeability describes the transport properties of a fluid passing through a connected pore space in, e.g., sedimentary rocks. Further, permeability is an intrinsic hydraulic material property and in the subsurface industry, a key parameter where reliable predictions are essential.

5.1 Klinkenberg corrected permeability

Permeability is in principle independent on properties of the flowing fluid, but experimental studies have shown a pore pressure dependency on gas permeability, k_g (the "Klinkenberg effect"). Klinkenberg (1941) suggested an empirical method for correction of k_g to the equivalent intrinsic liquid permeability. On various lithologies with different petrophysical characteristics, the correction method has been used in numerous studies and is the basis for theoretical or empirical modification (e.g., Sampath and Keighin, 1982; Civan, 2009; Tanikawa and Shimanoto, 2009; Moghadam and Chalaturnyk, 2015; Al-Jabri et al., 2015; Li and Sultan, 2017). For liquid flow, Poiseuille's law as implemented by Kozeny (Kozeny, 1927) considers zero velocity at the pore wall due to friction arising from the small molecular mean free path in the fluid (order of inter-molecule distance) and consequently inter-molecular collisions are dominating the liquid flow. On the other hand, for gas flow, Klinkenberg (1941) argued that a non-zero gas velocity at the pore wall for a given pressure gradient causes a higher permeability compared to the equivalent liquid permeability (Klinkenberg, 1941). Klinkenberg proposed to derive the equivalent liquid permeability (Klinkenberg corrected permeability, k_K), by theoretically extrapolating the mean free path of the applied gas to that of a liquid and accordingly utilize the pressure dependence on the mean free path. Klinkenberg derived k_g from the classical Darcy's law at a series of pressures and made a linear correlation of k_g versus the inverse mean pressure ($1/P_m$) and by extrapolating to zero $1/P_m$ determined the equivalent liquid permeability (k_K). The validity of Darcy's law for deriving k_g is however inherent to the procedure, in practice meaning laminar flow conditions and a linear flow versus pressure relation.

5.2 Reynolds number in porous media

The Reynolds number (*Re*) defines the inertia to viscous force ratio and are in hydraulics commonly used to distinguish laminar and turbulent flow conditions. However, between the laminar and the turbulent flow conditions, there is a transition zone, where the flow is laminar but non-linear, and the classical Darcy's law no longer is valid. *Re* is for a conduit derived from the hydraulic diameter, d, fluid discharge Q, fluid density ρ_f and dynamic fluid viscosity μ. The interstitial Reynolds number (Re_{app}) expressed by Huang and Ayoub, 2008 for a porous medium is:

$$Re_{app} = \frac{\rho_f q d_{app}}{\mu}, \tag{5.1}$$

where the hydraulic diameter (d) is substituted by an apparent length scale (d_{app}), in principle characterizing the pore diameter, and q is the average flux, typically determined from measured discharge, cross sectional area, A, and porosity, ϕ ($q = Q/A\phi^{-1}$). The flow is essentially laminar as well as with a linear relation between discharge and pressure leading to the validity of Darcy's law when Re_{app} do not exceed some value between 1 and 10 (Scheidegger, 1960 and Bear, 1972).

5.3 Modelling permeability from Kozeny's equation and NMR

The permeability in a homogenous sedimentary rock relates to the specific surface and porosity in accordance with Kozeny (1927) as:

$$k = c\frac{\phi}{S_P^2}, \tag{5.2}$$

where S_P is the specific surface respect to the pores. Kozeny defined c as an empirical parameter, in practice accounting for the geometry of the pore space, including flow obstruction as well as heterogeneity. By envisaging the pore space as orthogonally arranged and interpenetrating conduits constituting the total porosity, Mortensen et al. (1998) applied Poiseuille's law to derive an expression for Kozeny's factor, c_M, assuming a homogenous distribution of specific surface. Accounting only for the shielding effect obstructing fluid flow the factor by Mortensen et al. (1998) is denoted shielding factor and for a circular conduit expressed as:

$$c_M = \left\{ 4\cos\left[\frac{1}{3}\arccos\left(\phi \frac{64}{\pi^3} - 1 \right) + \frac{4\pi}{3} \right] + 4 \right\}^{-1}. \quad (5.3)$$

The expression in equation 5.3 approximates a linear relation for porosities of interest to most sandstones and simplifies to (Orlander et al., II):

$$c_M = 0.155\phi + 0.175, \ \phi < 0.4. \quad (5.4)$$

Assuming surface contributions (interactions between the pore fluid and pore surface) as the dominating the transverse NMR relaxation, thus neglecting contributions from bulk relaxation in the fluid and molecular diffusion due to in-homogeneity of the magnetic field, the total transverse NMR relaxation, T_2, reduces to:

$$\frac{1}{T_2} \approx \rho_2 S_{\mathrm{P}} \quad (5.5)$$

where ρ_2 is the surface relaxivity related to the solid surface. By combining equation 5.2, 5.5 in accordance with Hossain et al. (2011) and thus substituting c with c_{M} as well as expanding the expression to represent incremental permeability contributions from individual pore sizes, the incremental NMR permeability is expressed as:

$$k_{\mathrm{NMR},i} = c_{\mathrm{M}} \phi f_{\mathrm{NMR},i} (T_{2,i}\rho_2)^2, \quad (5.6)$$

where, $f_{\mathrm{NMR},i}$ is the fraction of the porosity corresponding to $T_{2,i}$. The incremental porosity, $\phi'_{\mathrm{inc,NMR}}$, is defined as $\phi f_{\mathrm{NMR},i}$. Summation of individual $k_{\mathrm{NMR},i}$ from the smallest pore define the cumulated permeability $k_{\mathrm{NMR,cum}}$ and by assuming cylindrical pores, the pore size from NMR T_2 relaxation time is expressed as:

$$\frac{1}{T_2} = \rho_2 S_{\mathrm{P}} = \rho_2 \left(\frac{2\pi r l}{\pi r^2 l} \right) = \rho_2 \frac{4}{d_{\mathrm{NMR}}} \Leftrightarrow d_{\mathrm{NMR}} = 4\rho_2 T_2, \quad (5.7)$$

where r is the pore radius, l is the pore length, and d_{NMR} is the pore diameter.

5.4 Application of Klinkenberg's suggested practice on sandstones

On a series of outcrop sandstones from Fontainebleau, Obernkirchen, Castlegate, and Bentheim (See chapter 2 for characteristics), the applicability of Klinkenberg's original

method (section 5.1) for correction of gas permeability to the apparent liquid permeability of sandstones was investigated from liquid and gaseous flow-through experiments.

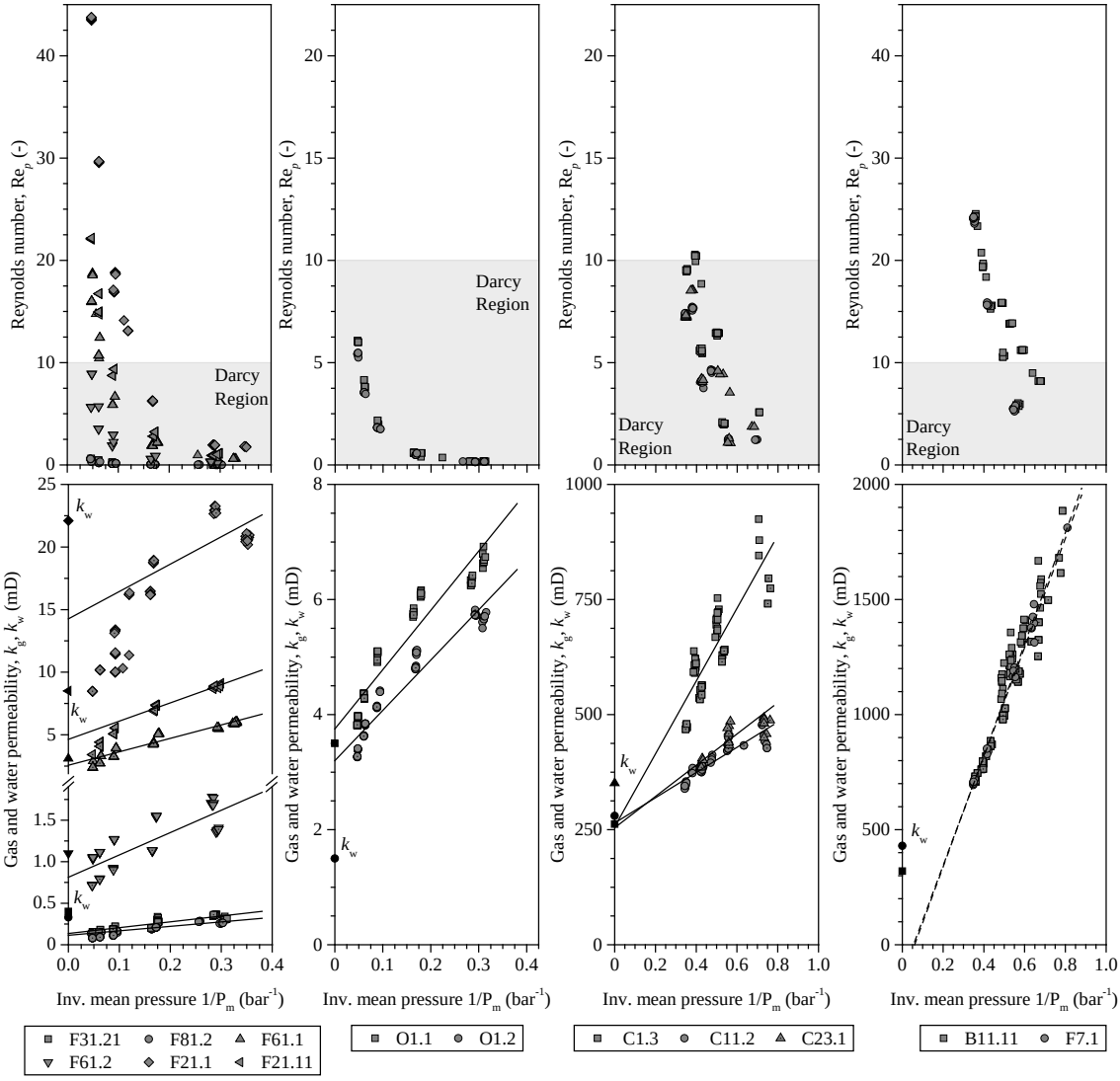

Figure 5.1. 1st row) Reynolds number versus inverse mean pressure. Marking with F is Fontainebleau samples, O is Obernkirchen, C is Castlegate and B is Bentheimer. Data are from Orlander et al., II. The regions with Darcy conditions is marked in grey. 2nd row) Gas permeability versus inverse mean pressure defined as the mean of up and down stream pressure. Black markers are water permeability plotted at $1/P_m = 0$.

By taking into account, the constraints of valid Darcy condition, gas permeability, k_g, was derived from Darcy's law and the equivalent liquid permeability, k_K from Klinkenberg correction. However, it is not common practice to envisage the inherent constraints of applying Darcy law in flow-through experiments with gaseous fluids, but it was done in

studies by Bloomfield and Williams (1995), as well as Huang and Ayoub (2008). The frequent failure to envisage the constraints of Darcy's law indirectly influences the procedure of Klinkenberg correction and consequently induce a risk of misinterpreted results.

Reynolds number was in this study estimated from equation 5.1 with input of d_{app} from an apparent pore size determined from BSEM images of the studied material. The derived Reynolds numbers indicate laminar gas flow for all Obernkirchen and Castlegate samples, but three Fontainebleau samples with porosity and k_g above 0.05 and 2 mD respectively, show turbulence at the highest mean pressures (Figure 5.1 1st. row). The gas permeability derived for sample F7.1 and B11.11 only obeys the Darcy conditions at the lowest mean pressure, and consequently, the definition of a Klinkenberg corrected permeability is unfeasible (Figure 5.1 1st row). Results from sample F7.1 and B11.11 illustrate the importance of screening data of gas permeability for constraints to Darcy law and especially in high permeable material (>100 mD) where high specific fluid discharge caused by a high mean pressure increases the risk of laminar but non-linear or turbulent flow conditions.

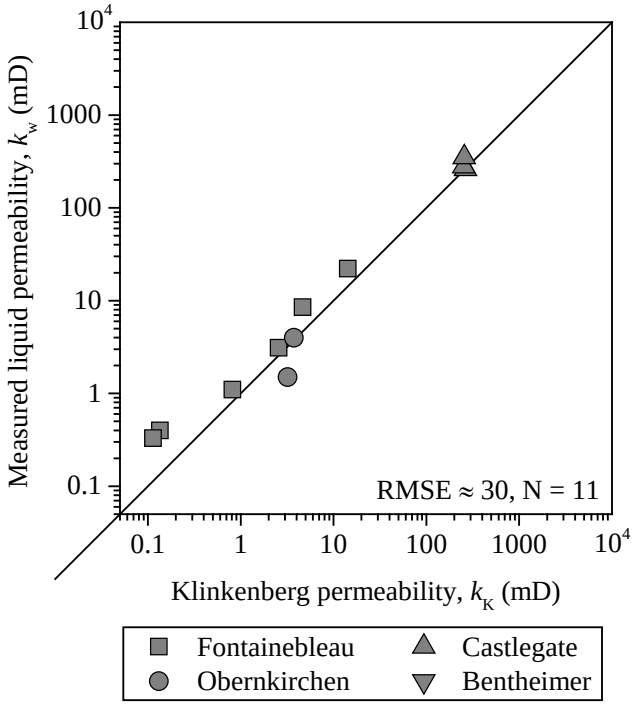

Figure 5.2. Cross plot of water permeability and Klinkenberg permeability. Data are from Orlander et al., II. Because of undefined k_K sample F7.1 and B11.11 are not shown.

Comparing liquid/water permeability (k_w) from flow-through experiments to the Klinkenberg corrected permeability k_K derived from data sampled in agreement with the constraints to Darcy's law (Figure 5.1 2nd row) shows good agreement and illustrates the capability of the suggested practice by Klinkenberg for sandstones (Figure 5.2). However, the findings of Figure 5.1 shows the necessity of extreme care in the evaluation of flow experiments with a high specific fluid discharge.

Bourbié and Zinszner (1985) derived gas (air) permeability on a series of Fontainebleau samples with a wide porosity range and implied Klinkenberg correction as insignificant, thus assuming measured gas permeability equal to the liquid ($k_g = k_w$). Revil et al. (2014) likewise derived permeability from gas measurements on Fontainebleau samples with an identical porosity range, but stated use of Klinkenberg correction, so results in principle represent k_w ($k_K = k_w$). However, results obtained by Bourbié and Zinszner (1985) and Revil et al. (2014) are identical (Figure 5.3) illustrating a discrepancy with respect to application of Klinkenberg correction.

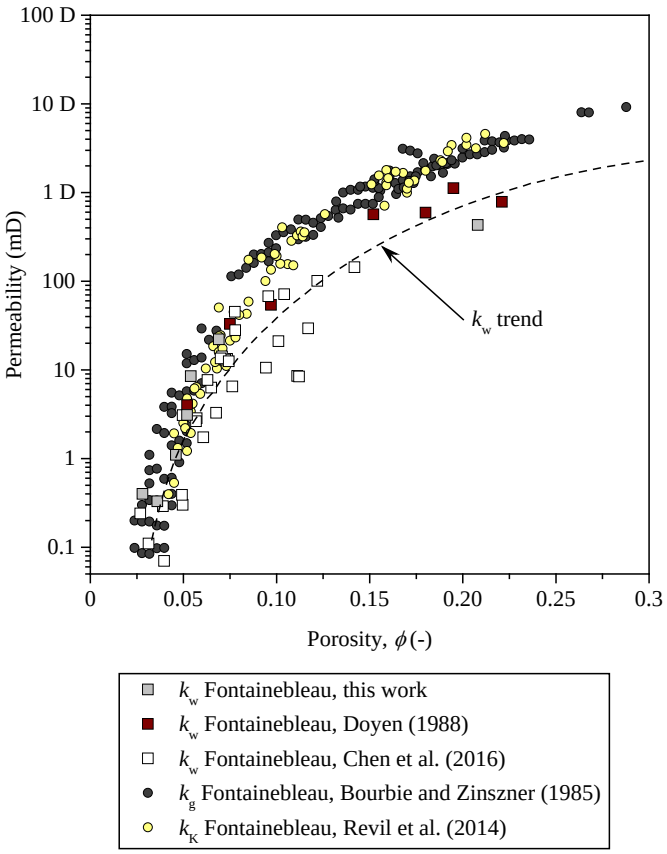

Figure 5.3. Cross plot of permeability and porosity. Comparison of studies on Fontainebleau. Dashed line is a feasible fit based on measured liquid permeability.

The results of k_g and k_K obtained by Bourbié and Zinszner (1985) and Revil et al. (2014) respectively do not include supporting measurements of k_w and comparing results to measurements of k_w on Fontainebleau sandstones from Doyen (1988), Chen et al. (2016) show k_K and k_g to be significantly higher than of k_w (Figure 5.3). However, the tendency is pronounced at porosities above 0.1, whereas for porosities below 0.1 the agreement between gas and liquid permeability is good (Figure 5.3).

A more feasible porosity-permeability trend appears less steep than results by Bourbié and Zinszner (1985) and Revil et al. (2014) when based on flow-through experiments using liquid (Figure 5.3) and the discrepancy of k_g, $k_K > k_w$ at $\phi > 0.1$ is presumably related to one or more causes where the authors: 1) omitted to confirm the presence of valid Darcy conditions in flow-through experiments; 2) applied a too narrow range of mean pressures for classical Klinkenberg correction; or 3) applied an unsuitable empirical relation to the gas permeability. Application of empirical relations inherently implies caution, whereas omitting to confirm presence of valid Darcy conditions or using a too narrow range of mean pressures in experiments, emphasize screening of results for valid Darcy conditions by Reynolds number and pore size estimation from, e.g., BSEM images.

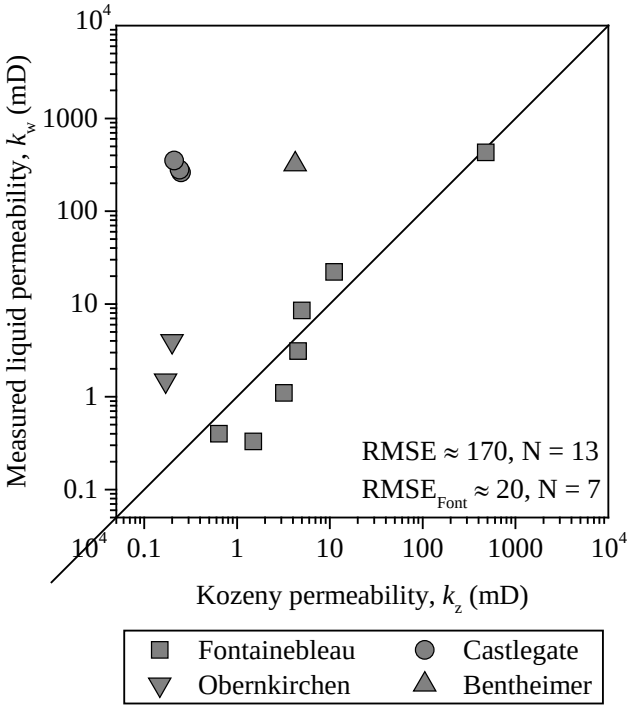

Figure 5.4. Cross plot of water permeability and permeability predicted from Kozeny's equation. Data are from Orlander et al., II. $RMSE_{font}$ is derived using Fontainebleau samples.

Applying S_P derived from BET measurements (Table 2.4) as well as c_M calculated from equation 5.3 for prediction of permeability from Kozeny's equation (equation 5.2) on the same series of sandstones (Figure 5.1 and 5.2) show for Fontainebleau samples good agreement with liquid permeability (Figure 5.4). For the clay-free Fontainebleau samples the agreement between predictions from Kozeny (k_z) and measurements (k_w) are presumably related to a homogenously distributed specific surface, in accordance with the pre-conditions of both Kozeny's equation and c_M. For the clay containing samples, the predicted Kozeny permeability is however significantly lower than k_w (Figure 5.4). The offset is presumably related to overestimated S_P from BET because of heterogeneously distributed clay causing violation of the pre-condition adherent to Kozeny's equation. The surplus specific surface (S_P) leading to $k_z < k_w$ defines small pores in isolated areas that do not contribute significantly to permeability corresponding to findings from cumulated NMR permeability ($k_{NMR,cum}$), where the contribution from pores smaller than 0.1 μm is below 10^{-4} mD (Figure 5.5 showing examples).

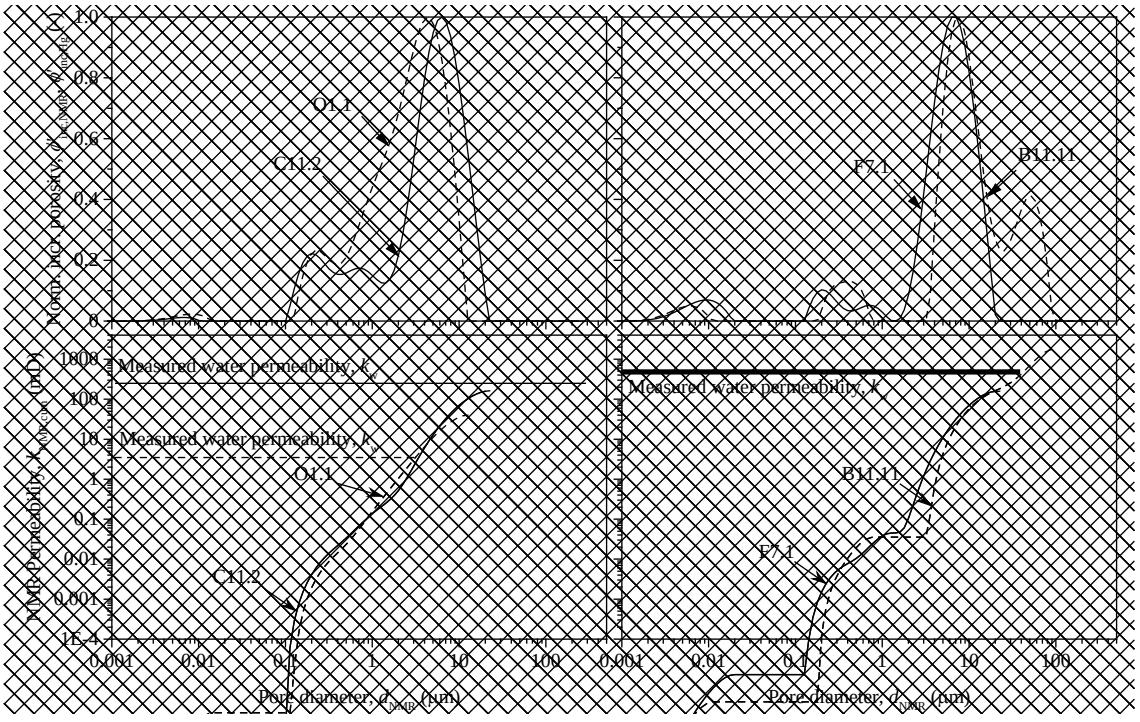

Figure 5.5. Summarized plot of selected samples, using 10 μm/s Upper graphs show normalized incremental porosity versus NMR pore diameter using surface. Lower graphs shows incremental and cumulated NMR permeability versus NMR pore diameter. Markings with F is Fontainebleau samples, O is Obernkirchen, C is Castlegate and B is Bentheimer. Data are from Orlander et al., II. Measured water permeability, k_w, is plotted as a horizontal line. Scratched area, is representing pore sizes cumulated from the smallest to $k_{NMR,cum} = k_w$.

For Castlegate samples with the highest specific surface (Table 2.4), the specific surface of all pores controlling the permeability (i.e., except the isolated small pores) is relevant, because the full range of pore sizes is required for $k_{NMR,cum}$ to equal k_w (Figure 5.5). For $k_{NMR,cum}$ to equal k_w in the Obernkirchen samples requires only pores smaller than 3 μm, so the largest pores do not contribute to the permeability. However, the controlling surface is heterogeneously distributed, and the derived Kozeny permeability is an order of size smaller than the measured liquid permeability (Figure 5.4).

Comparing pore size distributions and $k_{NMR,cum}$ of sample F7.1 and B11.11, the two samples appear identical below a pore size of 20-30 μm (Figure 5.5). B11.11 have larger pores, however these do not contribute to permeability (Figure 5.5) because the larger pores are obstructed by the smaller and thus do not form a continuous path in the pore space. Consequently, fluid flow in sandstones is controlled by the smaller pores, and opposite to the common NMR practice, the large ineffective pores should be cut-off from the smaller pores.

6. MODELLING OF THERMAL CONDUCTIVITY IN SANDSTONES

Assessment of depth variations in thermal conductivity are often limited to estimations from downhole logging data because of minimal access to core material. However, as standard logging campaigns do not yet include tools for in-situ measurements of thermal conductivity (e.g., Freifeld et al. 2008 and Moscoso Lembcke et al. 2016) estimation of the thermal conductivity from empirical relations or theoretical models based on other formation characteristics is required. Hartmann et al. (2005), as well as Fuchs and Förster (2014), published empirical work on logging based predictions of thermal conductivity, but the inherent constraints of empirical relations suggest great caution. Studies on modelling of thermal conductivity, λ, are numerous and include both theoretical and empirical models (Abdulagatova et al., 2009). Examining the literature, one finds that the theoretical models of λ use porosity, ϕ, as a key input parameter and provided knowledge of the constituents' thermal conductivity; porosity also governs the theoretical bounds denoted as Wiener bounds (Wiener, 1904). The Wiener bounds are however only capturing a bare minimum of the rock texture from porosity and are generally too wide for practical use. Consequently, the geometric mean is commonly applied despite lacking physical meaning (e.g., Woodside and Messner, 1961a; Woodside and Messner, 1961b; Sass et al., 1971; Brigaud and Vasseur, 1989 and Troschke and Burkhardt, 1998) and is regarded as a good approximation. Further, the geometric mean is often applied as a mixing law for computation of the overall solid thermal conductivity (e.g., Fuchs and Förster, 2014). For isotropic and homogenous mixtures, Hashin and Shtrikman (1962) formulated more narrow bounds than the Wiener bounds (Zimmerman, 1989), and these are considered the most reliable bounds solely based on porosity and constituent thermal conductivity. Quantifying rock texture of a sedimentary rock solely through volume fractions (ϕ) gives an incomplete picture and consequently several studies relate effects of constituent texture (e.g., pore geometry, grain size and grain shape, etc.) on the overall thermal conductivity (e.g. Huang, 1971; Midttomme and Roaldset, 1998; Revil, 2000). However, because pores and solids are smaller than a representative volume, emphasis should be on describing the cross sections between single pores and solids. Studies relating electrical resistivity (e.g., Revil, 2000) or elastic wave velocity (e.g., Horai and Simmons, 1969; Zamora et al., 1993; Kazatchenko et al., 2006) to thermal conductivity, indirectly relate cross sections of pores and solids respectively to the overall thermal

conductivity, and consequently predictions from these models are able to match specific data sets. The thermal conductivity of the solid constituents is in most sandstones several orders of size larger than that of the saturating fluid (water, for most practical applications) emphasizing quantification of the cross-section governing heat transfer between solids (grains). Studies by, e.g., Deissler and Eian (1952), Kunii and Smith (1959), Woodside and Messmer (1961b), Batchelor and O'Brien (1977), Hadley (1985), and Hsu et al. (1994) evaluated the cross section governing solid heat transfer as particle to particle contacts, but addressed quantification through geometrical simplification of the solid rock texture, thus setting constraints on the particle shape. Other studies on thermal conductivity, e.g., Gegenhuber and Schoen (2012) and Pimienta et al. (2014) envisage sedimentary rocks as a continuous but porous and/or cracked mineral leading to a concept where the solid contacts are only addressed through mathematical modelling. Studies by, e.g., Woodside and Messner (1961a), Huang (1971) as well as Tarnewski and Leong (2012), divided a one-dimensional heat transfer through a sedimentary rock into three parallel heat transfer paths of solid, fluid, and solid-fluid in series, to represent individual contribution from the rock texture. This concept of parallel heat paths is the basis for establishment of a new thermal conductivity model where three parallel heat paths are constrained in a unit volume. Cross sections governing the three heat paths in this new model quantified through Biot's coefficient and c_{M} from Kozeny, in order to capture the rock texture.

6.1 A new model of thermal conductivity from α and c_{M}

Following studies relating measures of frame stiffness to thermal conductivity (e.g., Horai and Simmons, 1969; Zamora et al., 1993; Kazatchenko et al., 2006; Gegenhuber and Schoen, 2012; and Pimienta et al., 2014), the cross section that governs heat transfer through the solid constituent is assumed equal to $(1 - \alpha)$ (section 3.1.1). The cross section of solid heat transfer can thus be derived from bulk density, and elastic wave velocities provided knowledge of constituting mineralogy (section 3.1). The cross-section governing heat transfer through the pore space in one direction in line with Poiseuille's law is quantified by c_{M} from section 5.3 by assuming that the cross section governing heat transfer, as well as fluid flow are equal. The cross section governing heat transfer through the pore space is then $c_{\mathrm{M}}\phi$ and thus a simple function of porosity.

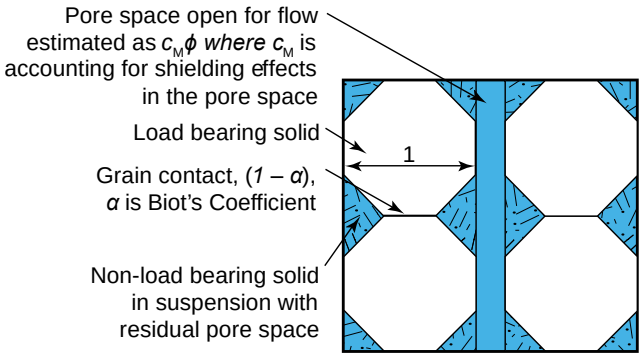

Figure 6.1. Conceptual illustration of a sandstone with distribution of minerals.

A model of thermal conductivity based on the conceptual simplification of a sandstone (Figure 6.1) is established by acknowledging that most sandstones consist of several minerals, but only one load bearing (Figure 6.1). V_{sus} defines the non-load bearing fraction of the total solid volume and is assumed to be suspended in the pore space between the load bearing mineral (Figure 6.1). Assuming a purely conductive heat flow, thus neglecting presumably minor contributions from convection and radiation, the solid and fluid constituents in the inherent constraints of a unit cell are distributed in three parallel heat paths (Figure 6.2). The cross section of solid heat transfer (the cemented area) is in the established model quantified as $(1 - \alpha)$ whereas the cross section of heat transfer through the pore space as $c_M\phi$ (Figure 6.2). Using ϕ as a quantity of the total pore volume and $(1 - \phi)$ as the total solid volume the residual volumes of pores and solid are $(\alpha - \phi)$ and $(1 - c_M)\phi$ respectively. The residual load bearing solid from $(\alpha - \phi)$, is thus $(\alpha - \phi - V_{sus})$, and arranged in series with V_{sus} and the residual pore space (Figure 6.2, central heat path). Assuming a constant thermal conductivity of each constituent, and summarizing contribution from the established distribution of constituents, the overall (effective) thermal conductivity λ is:

$$\lambda = (1-\alpha)\lambda_{lbs} + c_M\phi\lambda_f + (\alpha - c_M\phi)^2\left(\frac{(1-c_M)\phi}{\lambda_f} + \frac{V_{sus}}{\lambda_{sus}} + \frac{\alpha-\phi-V_{sus}}{\lambda_{lbs}}\right)^{-1}, \quad (6.1)$$

$$(\alpha - \phi - V_{sus}) \geq 0,$$

where, λ_{lbs}, λ_{sus}, λ_f are thermal conductivities of the load bearing solid, the suspended non-load bearing solid, and the saturating liquid or gaseous fluid respectively. The volume V_{sus} includes all suspended solids in accordance with

$$V_{sus} = \sum_{i=1}^{n} V_{sol,i} \text{ and } \lambda_{sus} = \sum_{i=1}^{n} \lambda_{sol,i} \quad (6.2)$$

where V_{sol}, λ_{sol}, n and i are solid volume, solid thermal conductivity, the total number of non-load bearing solids and the i^{th} solid, respectively.

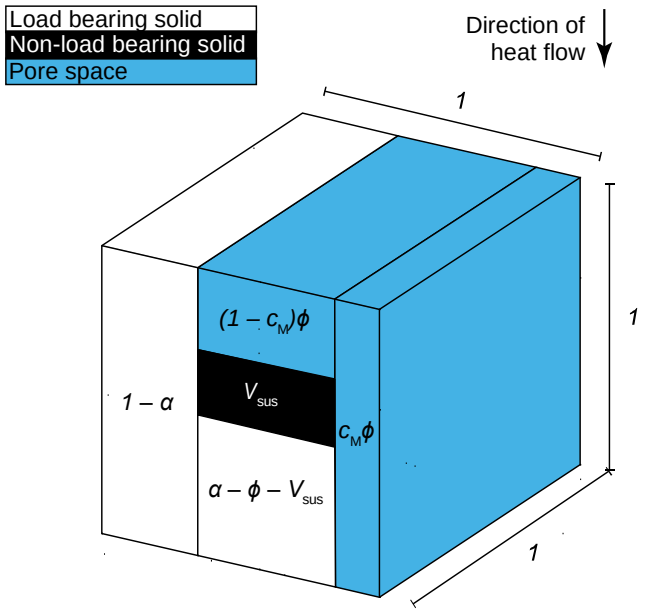

Figure 6.2. Partitioned rock unit volume showing the distribution of the load-bearing solid, the non-load bearing solid, connected pore space, and the residual pore space.

6.2 Model validation

The established model of thermal conductivity is in principle free of empirical constrains and constructed such that input may be quantified from standard well log data (e.g., ultrasonic velocity, density, neutron, Gamma Ray, and electrical resistivity). Further, provided knowledge or estimates of the mineralogy, the model uses a minimum number of input parameters to describe the texture of the modelled rock (section 6.1). In order to judge the ability of the established model to predict thermal conductivity with sufficient accuracy independent of saturating fluid, model predictions were validated from data of a series of sandstones identical to the ones used in the previous permeability study, as well as from a set of log data from the Gassum Formation. Laboratory data were compared to the conventional porosity-based bounds and geometric mean by Wiener and Hashin-Shtrikman, by assuming a solid constituent thermal conductivity of quartz, λ_S (Chapter 2), and fluid constituents of air, λ_A, and water, λ_W, for the dry and water saturated

case respectively. Collected data of porosity and thermal conductivity, in general plot within the Hashin-Shtrikman bounds and the geometric mean provides a good approximation. However, data also show that the thermal conductivity found in sandstone cannot in both the dry and water saturated case be captured by the geometric mean (Figure 6.3). Four Fontainebleau samples are outliers; presumably related to insufficient surface contact between the sample materials and measuring sensor as a consequence of weathered grain contacts (Figure 2.2 and 6.3). For these specific samples, data thus represent a material intermediate between sand and sandstone.

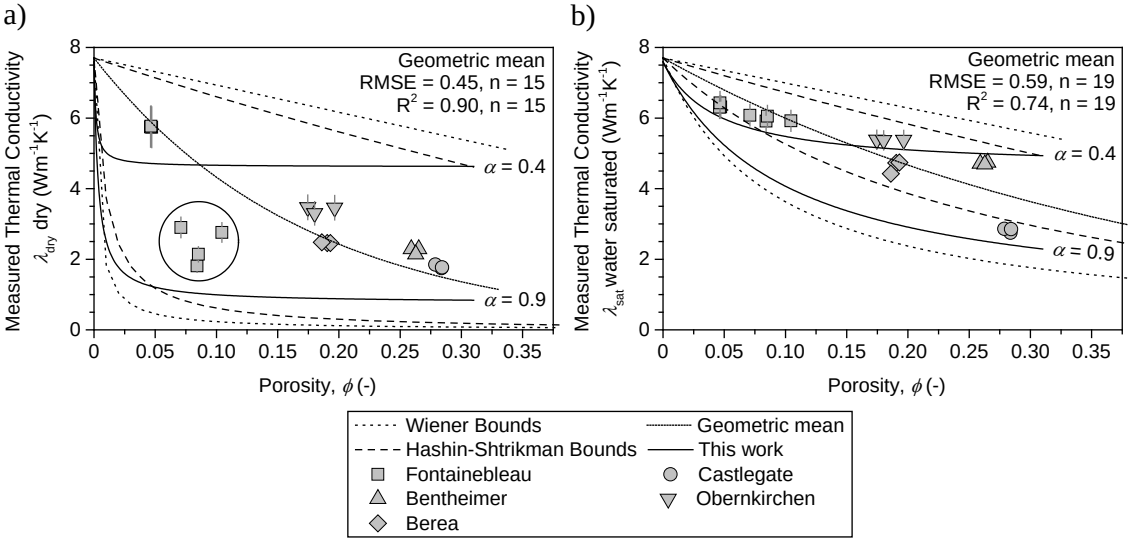

Figure 6.3. Thermal conductivity versus porosity cross plots of outcrop sandstones. Data are from Orlander et al., III. Out-liers (Fontainebleau) are marked with a circle and not included in derived regression data. Bounds are calculated using thermal conductivity of λ_S = 7.7 Wm^{-1}K^{-1}, λ_A = 0.024 Wm^{-1}K^{-1} and λ_W = 0.62 Wm^{-1}K^{-1} (Clauser and Huenges, 1995; Beck, 1976). a) in the dry state, b) in the water saturated state.

Data of thermal conductivity were plotted versus Biot's coefficient, in order to illustrate the relation between rock stiffness and thermal conductivity. Results show a decreasing thermal conductivity for increasing Biot's coefficient and consequently decreased thermal conductivity for decreasing grain contact area ($1 - \alpha$) (Figure 6.4). At the applied boundary conditions (see Figure 6.4) the solid heat transfer cross section is equal to the grain contact area, justifying the use of material stiffness for prediction of thermal conductivity as proposed by, e.g., Horai and Simmons (1969); Zamora et al. (1993); Kazatchenko et al. (2006); Gegenhuber and Schoen (2012) and Pimienta et al. (2014).

The general trends of thermal conductivity versus Biot's coefficient are different for the dry and water saturated case, indicating a significant contribution from the saturating fluid are and a single empirical relation can hence not capture both the dry and saturated case (Figure 6.4).

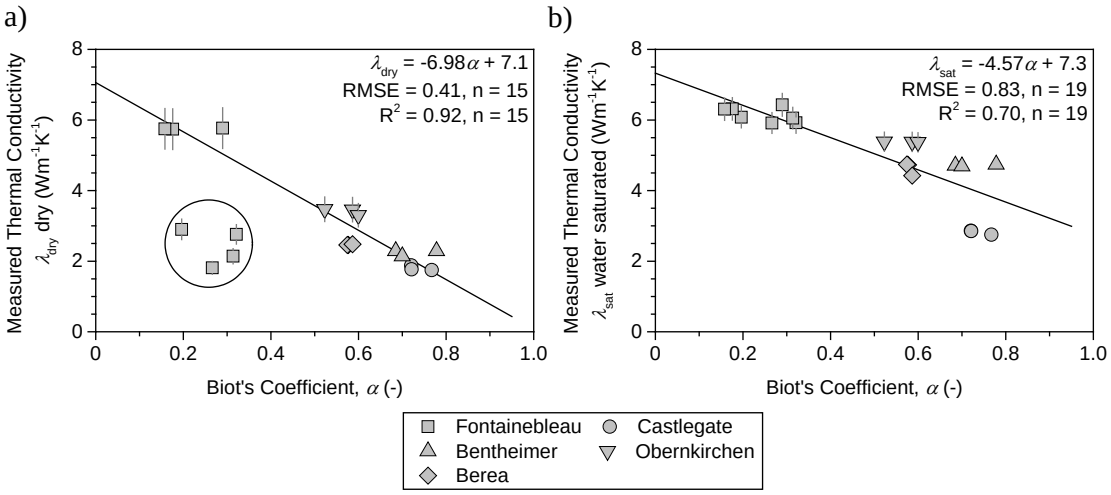

Figure 6.4. Measured thermal conductivity versus Biot's coefficient cross plots of outcrop sandstones. Thermal conductivity is measured at ambient pressure, and Biot's coefficient is derived at hydrostatic stress of 40 MPa using dry density and ultrasonic velocities (section 3.1). Data are from Orlander et al., III. A quartz mineral stiffness K_{min} of 37 GPa (Carmichael, 1961) is assumed for all samples. Outliers indicated with a circle are not included in derived regression data. a) in the dry state, b) in the water saturated state.

Differences in trends of thermal conductivity versus Biot's coefficient consequently lead to introduction of the shielding factor, c_M, in order to capture contributions from the saturating fluid on the overall thermal conductivity (section 5.3, equation 5.3 and equation 6.1). Recalling, 1) that the heat transfer in the saturating fluid is assumed analog to fluid transfer, and 2) that permeability predictions from Kozeny's equation and c_M on the clay-free Fontainebleau sandstones showed good agreement with liquid permeability (Figure 5.4), corresponds to the agreement between model prediction of thermal conductivity from the established model and measurements (with the exception of weathered samples in the dry state) (Figure 6.5). However, clay containing samples likewise show good agreement, but comparing Root Mean Square Error (RMSE) from model prediction of the geometric mean and this work, the latter is the best (Figure 6.3 and 6.5) illustrating

c_M as a good measure of the cross section with heat transfer in the pore space of sandstones.

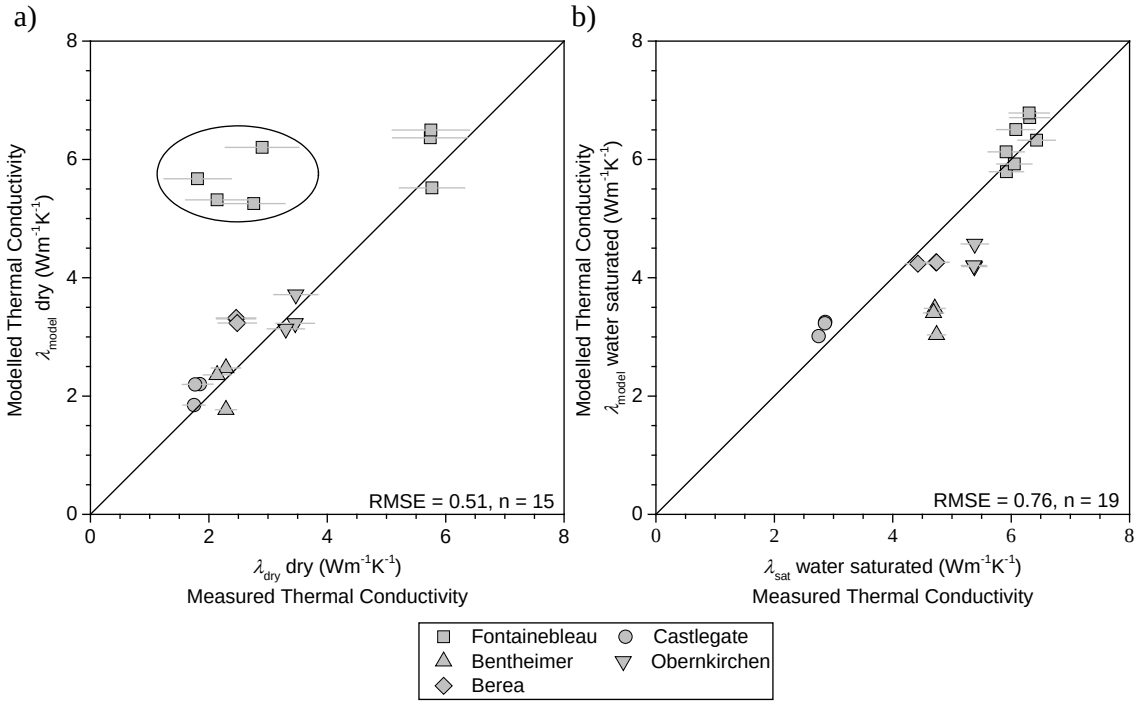

Figure 6.5. Modelled thermal conductivity (equation 6.1) versus measured thermal conductivity. Data are from Orlander et al., III. For the load bearing mineral and saturating fluid, thermal conductivities are identical to Figure 11.1. For non-load bearing clay minerals is a value of 6.0 $Wm^{-1}K^{-1}$ (after findings in Orlander et al., III) used. Volumes of V_{sus} were derived from Table 2.3. a) in the dry state, b) in the water saturated state.

Model predictions in Figure 6.5 correspond to maximum contact area between grain contacts (full closure of micro-cracks because of stress), whereas measurement of thermal conductivities conducted at atmospheric pressure represents the minimum contact area. The possibility for quantification of possible effects from discrepancies in boundary conditions is however not included in the data set. The magnitude of increased thermal conductivity from increased stress leading to increased solid contact area differs in literature. Horai and Susaki (1989) and Abdulagatova et al. (2009) showed an order of 0.1 $Wm^{-1}K^{-1}$ increase in thermal conductivity on sandstones following from a stress increase to 40 MPa, whereas Lin et al. (2011) showed an increase of 1 to 2 $Wm^{-1}K^{-1}$, but with a dependency of the saturating fluid. The stress effect on the thermal conductivity is presumably directly linked to closure of micro-cracks and thus to the material's geological stress and temperature history, emphasizing the importance of envisaging the

material's geological history in data evaluation.

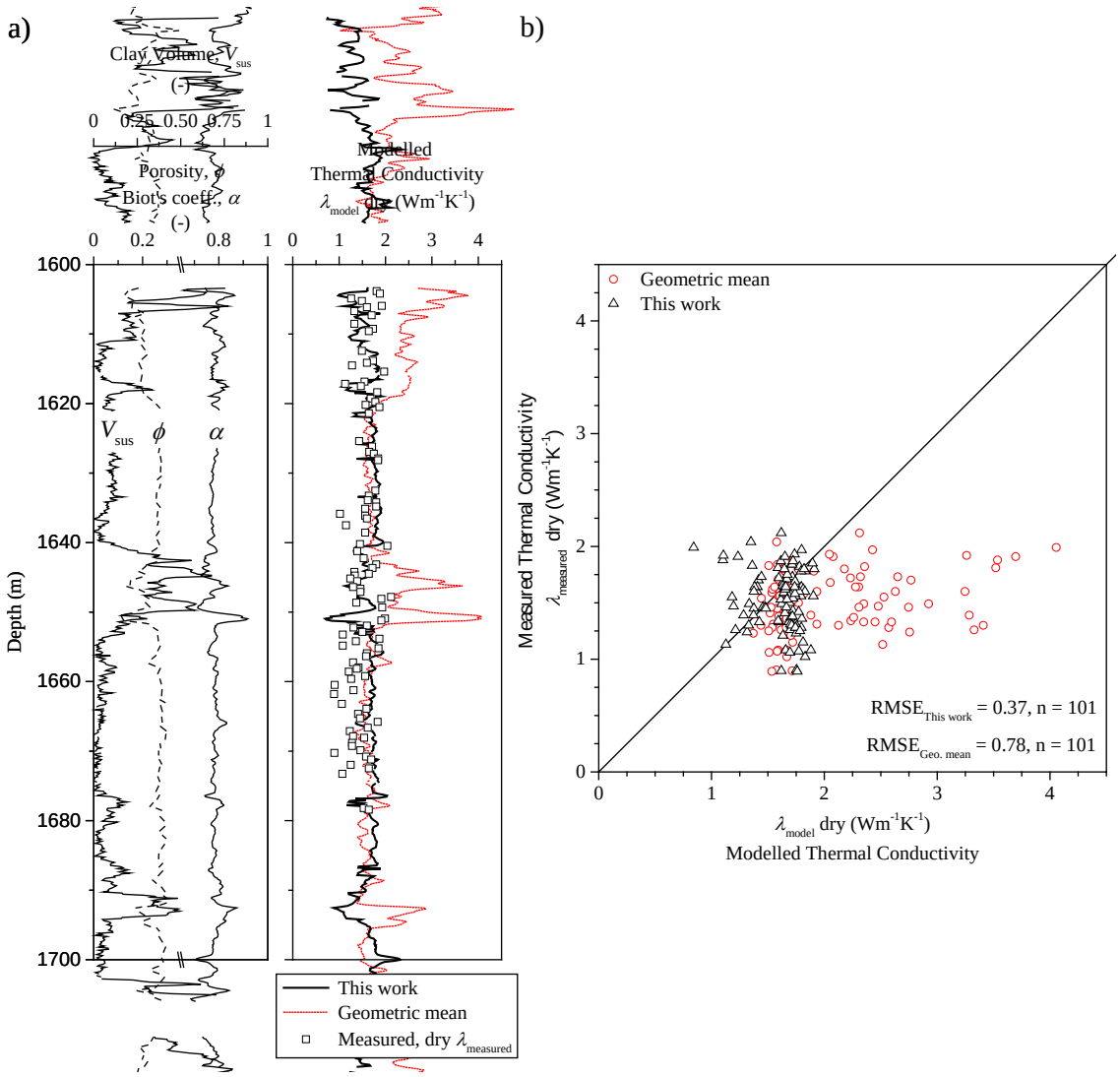

Figure 6.6. a) Depth plots of section from 1600 to 1700 meter showing porosity, Biot's coefficient and modelled thermal conductivities from geometric mean and this work. Data are from Orlander et al., III. a) In-situ porosity, Biot's coefficient clay volume, and thermal conductivity in the dry state. Further, with laboratory measured data points at ambient conditions. b) Measured thermal conductivity versus modelled thermal conductivity on Gassum sandstone. Round and squared markers show modelled results of respectively geometric mean and this work.

Using logging data and corresponding core material of the Gassum Formation from an exploration well located on mid Zealand, Denmark, the established model was further validated. Dominated by 85% quartz and small amounts of feldspar and kaolinite, the Gassum Formation consists of sandstone with a series of clayey interlayered sections (Kjøller et al. 2011). The Gassum sandstone is thus similar to studied outcrop sandstones

(Chapter 2.2). Values of α, ϕ, and V_{sus} derived using conventional log interpretation were, combined with assumptions of constituent thermal conductivity identical to that of the outcrop samples, used as model input for prediction of thermal conductivity as a function of depth (Figure 6.6a). Comparing model predictions to thermal conductivity measured on slabbed core material show good agreement between modelled and measured thermal conductivity (Figure 6.6b). In general, but especially in the clayey sandstone sections with low porosity (Figure 6.6a), model predictions of this work provide better estimates of dry thermal conductivity, compared to the geometrical mean. No data of saturated thermal conductivity are available, but results from the dry case illustrate the model applicability as well as the concept of including rock stiffness and permeability in modelling of thermal conductivity.

7. CONCLUSIONS

From a non-isothermal extension of Biot's original effective stress equation, the consequences for the subsurface effective stress are examined. From the simplified case study of deep North Sea basin, the effective stress estimated for isothermal conditions is presumably too high and the effective stress presumably neutral at large depth.

Experimental results of dynamic and static elastic modulus of dry sandstone show that increased testing temperature stiffens the dry rock frame of three types of sandstone from the deep North Sea basin by two controlling mechanisms. Both mechanisms are related to the thermal expansion of constituting minerals, and in principle governed by the total stress level. The resulting magnitude of stiffening effects is however different for the two mechanisms. At stress levels with partial micro-crack closure, thermally induced closure of micro-cracks showed stiffening of the rock frame, but the stiffening is minor and insignificant compared to micro-crack closure by stress increase. At stress levels where the sample volume is thermally constrained, thermally induced stiffening by conversion of thermal strain to stress leads to a significant overall stiffening of the rock frame. Further, at stress levels leading to a thermally constrained sample volume, thermally induced increase in internal stress results in increased shear resistance and thus strengthening of the sandstone material. Experimental results of stiffness and strength of dry rocks, envisaging the maximum in-situ temperature of the investigated material, showed both stiffening and strengthening for increased temperature, but it is emphasized that extreme care should be taken if result is used as trends for other materials. Further, results are obtained solely from tests in the dry state, and thus possible effects of the saturation fluid are not included.

The derived water and gas permeability from a sequence of liquid and gaseous flow through experiments on outcrop sandstones showed the applicability and importance of Klinkenberg correction, as well as validation of experimental flow conditions by use of Reynolds number. Reynolds number can with success be derived from an apparent pore size estimated from backscatter electron micrographs. Comparing measured liquid permeability to the permeability modelled from Kozeny's equation using specific surface, from BET measurement and a theoretically derived Kozeny factor, showed good

agreement on clay free samples, because of the homogeneously distributed specific surface.

By using NMR in combination with Kozeny's equation permeability contribution was modelled for each pore size. Cumulating modelled contributions from the smallest pores to equal the measured liquid permeability, showed that the larger pores do not form a continuous flow path and are insignificant for the overall permeability.

By using concepts from rock stiffness and permeability to quantify the rock texture a newly established model of thermal conductivity can provide predictions in good agreement with experimental results, using either laboratory or logging data as input. The established model is an improvement compared to conventional porosity-based models.

REFERENCES

Abdulagatova, Z., Abdulagatov, I.M., and Emirov, V.N., 2009, Effect of temperature and pressure on the thermal conductivity of sandstone: International Journal of Rock Mechanics and Mining Sciences, 46, 1055–1071.

Al-Jabri, R.A., Al-Maamari, R.S. and Wilson, O.B., 2015, Klinkenberg-corrected gas permeability correlation for Shuaiba carbonate formation: Journal of Petroleum Science and Engineering, 131, 172–176.

Alam, M.M., Fabricius, I.L. and Christensen, H.F., 2012, Static and dynamic effective stress coefficient of chalk: Geophysics, 77, L1–L11.

Banthia, B. S., King, M. S. and Fatt. I., 1965. Ultrasonic shear wave velocities in rocks subjected to simulated overburden pressure and internal pore pressure: Geophysics, 30, 117–121.

Batchelor, G.K., and O'Brien, R. W., 1977, Thermal or electrical conduction through a granular material: Proceedings of the Royal Society of London. Series, A. 355, 313–333.

Batzle, M and Wang, Z, 1992, Seismic properties of pore fluid, Geophysics, 57, 1396–1408.

Bear, J., 1972, Dynamics of Fluids in Porous Media, American Elsevier, New York.

Beck, A.E., 1976, An improved method of computing the thermal conductivity of fluid-filled sedimentary rocks: Geophysics, 41, 133–144.

Biot, M.A., 1941, General theory for three-dimensional consolidation: Journal of Applied Physics, 12, 155–164.

Bloomfield, J.P. and Williams, A.T., 1995, An empirical liquid permeability-gas permeability correlation for use in aquifer properties studies: Quarterly Journal of Engineering Geology, 28, S143–S150.

Bourbié, T., and B. Zinszner, 1985, Hydraulic and acoustic properties as a function of porosity in Fontainebleau sandstone: Journal of Geophysical Research, 90, 11524–11532.

Brigaud, F., and Vasseur, G., 1989, Mineralogy, porosity and fluid control on thermal conductivity of sedimentary rocks: Geophysical Journal, 98, 525–542.

Brunauer, S., Emmett, P.H. and Teller, E., 1938, Adsorption of gases in multimolecular layers: Journal of the American Chemical Society, 60, 309–319.

Carmichael, R.S., 1961, Practical Handbook of Physical Properties of Rocks and Minerals: Boca Raon, FL. CRC Press.

Chen, Y., 2016, Experimental study of the stress dependence of the permeability of rock, Geotechnical and Geological Engineering, 34, 1571–1575.

Civan, F., 2009. Effective correlation of apparent gas permeability in tight porous media: Transport in Porous Media, 82, 375–384.

Clauser, C., and Huenges, E., 1995, Thermal Conductivity of Rocks and Minerals, in Rock Physics and Phase Relations: A Handbook of Physical Constants, American Geophysical Union, Washington, D. C.

Deissler, R.D., and Eian, C.S., 1952, Investigation of effective thermal conductivity of powders: National Advisory Committee for Aeronautics, RM E52C05.

Doyen, P. M., 1988, Permeability, conductivity, and pore geometry of sandstone: Journal of Geophysical Research, 93, 7729–7740.

Fabricius, I.L., 2010, A mechanism for water weakening of elastic moduli and mechanical strength of chalk: 80th Annual International Meeting, SEG, Expanded Abstracts, 2736–2740.

Frempong, P., Donald, A. and Butt, S. D., 2007, The effect of pore pressure depletion and injection cycles on ultrasonic velocity and quality factor in a quartz sandstone: Geophysics, 72, E43–E51.

Freifeld, B.M., Finsterle, S., Onstott, T.C., Toole, P. and Pratt, L.M., 2008, Ground surface temperature reconstructions: Using in situ estimates for thermal conductivity acquired with a fibre-optic distributed thermal perturbation sensor: Geophysical Research Letters, 35, no. 14, L14309.

Fuchs, S., and Förster, A., 2014, Well-log based prediction of thermal conductivity of sedimentary successions: a case study from the North German Basin: Geophysical Journal International, 196, 291–311.

Gegenhuber, N., and Schoen, J., 2012, New approaches for the relationship between compressional wave velocity and thermal conductivity: Journal of Applied Geophysics, 76, 50–55.

Gommesen, L., Fabricius, I.L., Mukerji, T., Mavko, G. and Pedersen, J.M., 2007, Elastic behaviour of North Sea chalk: A well-log study: Geophysical Prospecting, 55, 307–322.

Hadley, G.R., 1986, Thermal conductivity of packed metal powders: International Journal of Heat Mass Transfer, 29, No. 6, 909–920.

Hajpál, M., 2002, Changes in Sandstones of Historical Monuments Exposed to Fire or High Temperature: Fire Technology, 38, 373–382.

Handin, J. and Hager, R.V., 1958. Experimental deformation of sedimentary rocks under confining pressure: Tests at high temperature: AAPG Bulletin, 42, 2892–2934.

Hartmann, A., Rath, V., and Clauser, C., 2005. Thermal conductivity from core and well log data: International Journal of Rock Mechanics and Mining Science, 42, 1042–1055.

Hashin, Z. and Shtrikman, S., 1962. A variational approach to the theory of the effective magnetic permeability of multiphase materials: Journal of Applied Physics, 33, no. 10, 3125–3131.

Hassanzadegan, A., Blöcher, G., Zimmermann, G. and Milsch, H., 2011. Thermoporoelastic properties of Flechtinger sandstone: International Journal of Rock Mechanics & Mining Sciences, 49, 94–104.

Holt, R., 1994, Effects of coring on petrophysical measurements: Proceedings, Society of Core Analysts International Symposium, SCA 9407, Stavanger, Norway, 77–86.

Horai, K., and Simmons, G., 1969, Thermal conductivity of rock-forming minerals: Earth and Planetary Science Letters, 6, 359–368.

Horai, K., and Susaki, J., 1989, The effect of pressure on the thermal conductivity of silicate rocks up to 12 kbar: Physics of the Earth and Planetary Interiors, 55, 292–305.

Hossain, Z., Grattoni, C.A., Solymar, M. and Fabricius, I.L., 2011. Petrophysical properties of greensand as predicted from NMR measurements: Petroleum Geoscience, 17, 111–125.

Huang, H and Ayoub, J.A., 2008, Applicability of the Forchheimer Equation for Non-Darcy Flow in Porous Media: SPE Journal, 13, 112–122.

Hughes, D.S. and Cross, J.H., 1951. Elastic wave velocity in rocks at high pressures and temperatures: Geophysics, 16, 577–593.

Hughes, D.S. and Kelly, J. L., 1952. Variation of elastic wave velocity with saturation in sandstone: Geophysics, 17, 739–752.

Huang, J.H., 1971, Effective Thermal Conductivity of Porous Rocks: Journal of Geophysical Research, 76, no. 26. 6420–6427.

Hsu, C.T., Cheng, P., and Wong, K.W., 1994, Modified Zehner-Schlunder models for stagnant thermal conductivity of porous media: International Journal of Heat Mass Transfer, **37**, no. 17, 2751–2759.

Jaeger, J.C., Cook, N.G.W., and Zimmerman, R.W., 2007. Fundamentals of rock mechanics. Fourth edition. Blackwell Publishing.

Johnson, W.h. and Parsons, W.H., 1944, Thermal expansion of concrete aggregate materials: Journal of Research of the National Bureau of Standards, 32, 101–126.

Kazatchenko, E., Markov, M., and Mousatov, A., 2006. Simulation of acoustic velocities, electrical and thermal conductivities using unified pore-structure model of double-porosity carbonate rocks: Journal of Applied Geophysics, 59, 16–35.

Kjøller, C., Weibel, R., Bateman, K., Laier, T., Nielsen, L.H., Frykman, P., and Springer, N., 2011, Geochemical impacts of CO_2 storage in saline aquifers with various mineralogy - results from laboratory experiments and reactive geochemical modelling: Energy Procedia, 4, 4724–4731.

Klinkenberg, L.J., 1941. The permeability of porous media to liquids and gases. American Petroleum Institute. Drilling and Production Practice, 200–213.

Kozeny, J., 1927, Über kapillare Leitung des Wassers im Boden: Sitzungsberichte der Wiener Akademie der Wissenschaften, 136, 271–306.

Kunii, D., and Smith, J.M., 1959, Heat Transfer Characteristics of Porous Rocks: A.I.Ch.E. Journal, **6**, no. 1, 71–77.

Mao, X.-b., Zhang, L.-y., Li, T.-z. and Liu, H.-s., 2009. Properties of failure mode and thermal damage for limestone at high temperature: Mining Science and Technology, 19, 290–294.

Mavko, G., Mukerji, T. and Dvorkin, J., 2009. The Rock Physics Handbook, 2nd ed. Cambridge University Press. New York, USA.

Mavko, G. and Vanorio, T., 2010. The influence of pore fluids and frequency on apparent effective stress behavior of seismic velocities: Geophysics, 75, N1–N7.

McKinstry, H.A., 1965, Thermal expansion of clay minerals: The American Mineralogist, 50, 212–222.

McTigue, D.F., 1986, Thermoelastic response of fluid-saturated porous rock: Journal of Geophysical Research, 91, 9533–9542.

Midttomme, K. and Roaldset, E., 1998, The effect of grain size on thermal conductivity of quartz sands and silts: Petroleum Geoscience, 4, 165–172.

Mobarak, S.A. and Somerton, W.H., 1971. The effect of temperature and pressure on wave velocities in porous rocks: SPE-3571.

Moghadam, A.A. and Chalaturnyk, R., 2014, Expansion of the Klinkenberg's slippage equation to low permeability porous media. International Journal of Coal Geology, 123, 2–9.

Mortensen, J., Engstrøm, F., and Lind, I., 1998, The relation among porosity, permeability, and the specific surface of chalk from the Gorm field, Danish North Sea: SPE Reservoir Evaluation and Engineering, 3, 245–251.

Moscoso Lembcke, L.G., Roubinet, D., Gidel, F., Irving. J., Pehme, P., Parker, B.L., 2016, Analytical analysis of borehole experiments for the estimation of subsurface thermal properties: Advances in Water Resources, 91, 88–103.

Nur, A. and Simmons, G., 1969. Stress-induced velocity anisotropy in rock: an experimental study: Journal of Geophysical Research, 74, 6667–6674.

Palciauskas, V.V. and Domenico, P.A., 1982, Characterization of drained and undrained response of thermally loaded repository rocks: Water Resources Research, 18, 281–290.

Peksa, A.E., Wolf, K.-H.A.A., Slob, E.C., Chmura, Ł., and Zitha, P.L.J., 2017, Original and pyrometamorphical altered Bentheimer sandstone; petrophysical properties, surface and dielectric behavior: Journal of Petroleum Science and Engineering, 149, 270–280.

Pimienta, L., Sarout, J., Esteban, L., and Delle Piane, C., 2014, Prediction of rocks thermal conductivity from seismic wave velocities mineralogy and microstructure: Geophysical Journal International, 97, 860–874.

Ranjith P.G., Daniel R., Chen, B.J. and Perera, M.S.A., 2012. Transformation plasticity and the effect of temperature on the mechanical behaviour of Hawkesbury sandstone at atmospheric pressure: Engineering Geology, 151, 120–127.

Rao, Q.-h, Wang, Z., Xie, H.-f. and Xie, Q., 2007. Experimental study of properties of sandstone at high temperature: Journal of Central South University of Technology, 14, 478–483.

Regel, J.B., Orozova-Bekkevold, I., Andreassen, K.A., Høegh van Gilse, N.C. and Fabricius, I.L., 2017, Effective stresses and shear failure pressure from in situ Biot's coefficient, Hejre Field, North Sea: Geophysical Prospecting, **65**, 808–822.

Revil. A., 2000, Thermal conductivity of unconsolidated sediments with geophysical applications: Journal of Geophysical Research Letter, 6, no. B7, 16.749–16.768.

Revil, A., Kessouri, P. and Torres-Verdín, C., 2014, Electrical conductivity, induced polarization, and permeability of the Fontainebleau sandstone: Geophysics, 79, D301–D318.

Sampath, K. and Keighin, C. W., 1982, Factors Affecting Gas Slippage in Tight Sandstones of Cretaceous Age in the Uinta Basin: Journal of Petroleum Technology, 34, 2715–2720.

Sass, J.H., Lachenbruch, A.H., and Munroe, R.J., 1971, Thermal Conductivity of Rocks from Measurements of Fragments and its Application to Heat-Flow Determination: Journal of Geophysical Research, 76, 3391–3401.

Scheidegger, A. E., 1960. The Physics of Flow Through Porous Media. University of Toronto Press, Toronto.

Tanikawa, W. and Shimanoto, T., 2009, Comparison of Klinkenberg corrected gas permeability and water permeability in sedimentary rocks: International Journal of Rock Mechanics & Mining Sciences, 46, 229–238.

Tarnawski, V.R. and Leong, W.H., 2012, A series-parallel model for estimating the thermal conductivity of unsaturated soils: International Journal of Thermophysics, 33, 1191–1218.

Timur, A., 1977. Temperature dependence of compressional and shear wave velocities in rocks: Geophysics, 42, 950–956.

Troschke, B., and Burkhardt, H., 1998, Thermal Conductivity Models for Two-Phase Systems: Physics and Chemistry of the Earth, 23, no. 3, 351–355.

Wiener, O., 1904, Lamellare Doppelbrechung: Phys. Z., 5, 332–338.

Woodside, W. and Messmer, J. H., 1961a, Thermal Conductivity of Porous Media. I. Unconsolidated sands: Journal of Applied Physics, 32, 1688–1699.

Woodside, W. and Messmer, J. H., 1961b, Thermal Conductivity of Porous Media. II. Consolidated rocks: Journal of Applied Physics, 32, 1699–1706.

Wu, B, King, M.S. and Hudson, J.A., 1991. Stress-induced Ultrasonic Wave Velocity Anisotropy in a sandstone: International Journal of Rock Mechanics and Mining Sciences & Geomechanics Abstracts, 28, 101–107.

Zamora, M., Vo-Thanh, D., Bienfait, G. and Poirier, J.P., 1993, An empirical relationship between thermal conductivity and elastic wave velocities in sandstone: Geophysical Research Letters, 16, 1679–1682.

Zhang, L., Mao, X.-b. and Lu, A., 2009. Experimental Study on the Mechanical Properties of Rocks at High Temperature: Science in China Series E: Technological Sciences, 52, 641–646.

Zimmerman, R.W., 1989, Thermal conductivity of fluid-saturated rocks: Journal of Petroleum Science and Engineering, 3, 219–227.

Wu, B, King, M.S. and Hudson, J.A., 1991. Stress-induced Ultrasonic Wave Velocity Anisotropy in a Sandstone: International Journal of Rock Mechanics and Mining Sciences & Geomechanics Abstracts, 28, 101–107.

Wu, G., Wang, Y., Swift, G. and Chen. J., 2013. Laboratory Investigation of the Effects of Temperature on the Mechanical Properties of Sandstone: Geotechnical and Geological Engineering, 31, 809–816.

APPENDIX I – Journal manuscripts

Orlander et al., I: *Effect of temperature on the subsurface effective stress and stiffness of sandstones from the deep North Sea Basin*

Authors	Orlander, T., Andreassen, K.A. and Fabricius, I.L
Journal	Geophysics
Covered in Chapters	3 and 4
Status	Submitted

Orlander et al., II: *Comparison of gas, Klinkenberg and liquid permeability - controlling pore size as defined from NMR and Kozeny's equatio*n

Authors	Orlander, T., Milsch. H. and Fabricius, I.L.
Journal	Geophysics
Covered in Chapters	5
Status	Submitted

Orlander et al., III: *Thermal conductivity of sandstones from Biot's coefficient*

Authors	Orlander, T., Adamopoulou, E., Asmussen, J.J., Marczyński, A.A., Milsch. H., Pasquinelli. L. and Fabricius, I.L.
Journal	Geophysics
Covered in Chapters	6
Status	Accepted

APPENDIX II – Supplementary contributions

Permeability in deep North Sea sandstones as predicted from NMR

Authors	Orlander, T., Enemark, K.D., Andreassen, K.A. and Fabricius, I.L
Submitted	4th International Workshop on Rock Physics, June 2017, Trondheim, Norway

Thermal conductivity of sedimentary rocks as function of Biot's coefficient

Authors	Orlander, T., Adamopoulou, E., Asmussen, J.J., Marczyński, A.A., Milsch. H., Pasquinelli. L. and Fabricius, I.L.
Submitted	Proceeding, 6th Biot Conference on Poromechanics 2017, Paris, France

Temperature Effects on Stiffness Moduli of Reservoir Sandstone from the Deep North Sea

Authors	Orlander, T., Andreassen, K.A. and Fabricius, I.L.
Submitted	Proceeding 51st US Rock Mechanics/Geomechanics Symposium, American Rock Mechanics Association, 17-106, San Francisco, US.

Using Biot's coefficient in estimation of thermal conductivity of sandstones

Authors	Orlander, T., Pasquinelli. L. and Fabricius, I.L
Submitted	SEG International Symposium on Energy Geotechnics 2018, Lausanne, Switzerland

Stiffening and strengthening by increased temperature of dry sandstones from the deep North Sea Basin

Authors	Orlander, T., Andreassen, K.A. and Fabricius, I.L
Submitted	EAGE Annual 80th Conference and Exhibition 2018, Copenhagen, Denmark

APPENDIX III – Experimental procedures

Sample preparation

Core plugs prepared from downhole sampled material were cored from a depth interval of 2-3 meters to secure maximum specimen similarity. All samples were cored and trimmed to the conventional plug size of approximate 1.5 inch (≈38 mm) diameter and twice the length (≈76 mm). For studies of thermal conductivity were core plugs likewise prepared to the conventional dimensions. For studies of permeability were core plugs prepared to a diameter of 25 mm and twice the length. For all plugs were end surfaces were paralleled and polished within 0.05 mm.

Soxhlet extraction cleaning

By Soxhlet extraction were core plugs from downhole-sampled material cleaned for salt using methanol and subsequently for hydrocarbons using toluene.

Mineralogical composition

The mineralogy of studied rock material was determined by X-Ray Diffraction (XRD) using Cu K-α radiation and a Philips PW 1830 diffractometer. Backscatter Electron Micrographs (BSEM) where recorded from polished thin sections and the XRD mineralogy corroborated by Energy Dispersive X-ray Spectroscopy (EDS) on the solid phases. The carbonate content was determined from crushed side-trims or plugs by HCl dissolution and NaOH titration.

Porosity and grain density

Nitrogen (N_2) porosity, ϕ_N, and grain density, ρ_s, were measured on oven dried (60°C) and equilibrated core plugs using a porosimeter from Vinci Technologies.

Specific surface area

From nitrogen absorption on side-trims was area to mass ratio, $S_{BET,}$ (specific surface) calculated by multi-point inversion (Brunauer et al., 1938). The specific surface with respect to the bulk volume, S_B, is derived from S_{BET}, porosity, ϕ, and grain density, ρ_s as:

$$S_B = S_{BET}\rho_s(1-\phi), \qquad \text{(AIII.1)}$$

which, with respect to the pore volume, equals

$$S_P = S_B / \phi . \qquad \text{(AIII.1)}$$

BET measurements were conducted using Autosorb iQ gas sorption system from Quantachrome Instruments.

Electrical resistivity

The electrical resistance was measured on brine saturated samples at ambient temperature, by connecting samples in electrical series with a variable resistor in a 1 kHz AC circuit of 5 volt (Figure I.1). As the electrical circuit consists of only two resistors, adjusting the variable resistor (R_1) such that the voltage drop across the sample is half the supply are the sample resistance equal to R_1 and the sample resistivity derived from sample length (L) and cross-sectional area (A) as:

$$\rho = R_1 \frac{A}{L} . \qquad \text{(6.3)}$$

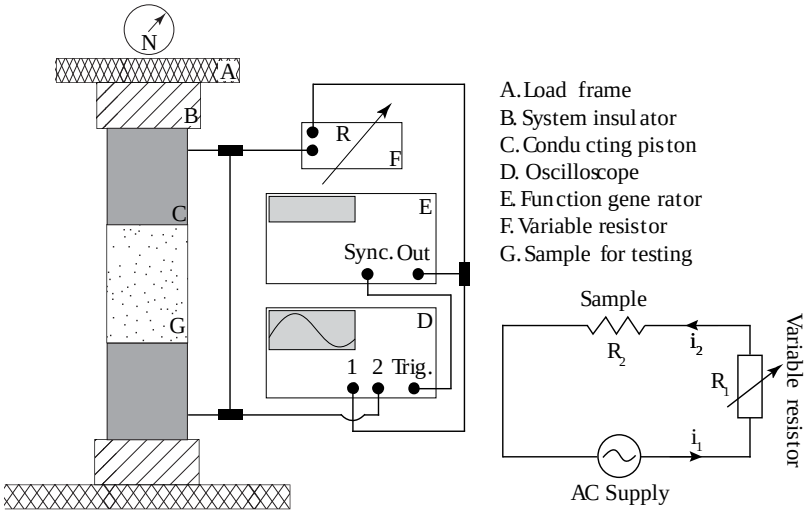

Figure III.1. Sketch of experimental setup for electrical resistance measurements.

Permeability

Gas permeability, k_g, of oven dried (60°C) samples were measured in a core holder designed for flow-through experiments at a 5 MPa confining stress. k_g was derived by applying Darcy's law on discharge and pressure data from flow-through experiments where argon gas flow was applying in the samples longitudinal direction. The discharge and pressure were measured at minimum three levels for each sample. The water permeability, k_w, of saturated plugs were likewise from Darcy's law and flow-through experiments.

Capillary pressure curves

Pressures and injected volumes of mercury in chips of dry side-trims, were recorded using a Poremaster® PM 33-GT-12, mercury porosimetry analyser for capillary pressure test and, converted to pore throat size using Washburn's equation.

Thermal conductivity

Using an ISOMET 2104 Heat Transfer Analyzer instrument from Applied Precision Ltd. (appliedp.com) was the dry thermal conductivity measured on core plugs in the dry state. On saturated samples was the saturated thermal conductivity measured using a C-Therm TCi instrument from C-THERM TECHNOLOGIES. Applied instruments both determined the thermal conductivity using a transient plane source placed directly on sample material at atmospheric pressure.

Low field NMR, T_2 distribution

On saturated samples using a GeoSpec2 NMR Core Analyzer at atmospheric pressure and a frequency of 2.25 MHz and 35°C temperature, was Nuclear Magnetic Resonance (NMR) measured with a recycle delay (repetition time) of 25 s, 16.000 echos and CPMG inter echo spacing (τ) of 50 μs using the Carr-Purcel-Meiboom-Gill (CPMG) pulse sequences. Using the WinDXP (Oxford Instruments UK) software was the NMR T_2 relaxations spectra derived.

Rock mechanical testing and static stiffness moduli

First arrival times of one ultrasonic compressional wave and two perpendicular shear waves, generated and received by piezoelectric transducers (Figure II.2) with a central frequency of 0.2 MHz and 0.5 MHz respectively was used to derive compressional and shear wave velocities. Rock mechanical properties of downhole sampled specimens were determined in a triaxial cell designed with temperature control from ambient to 200°C (Figure II.2). Rock mechanical properties of outcrop material were solely determined at ambient temperature.

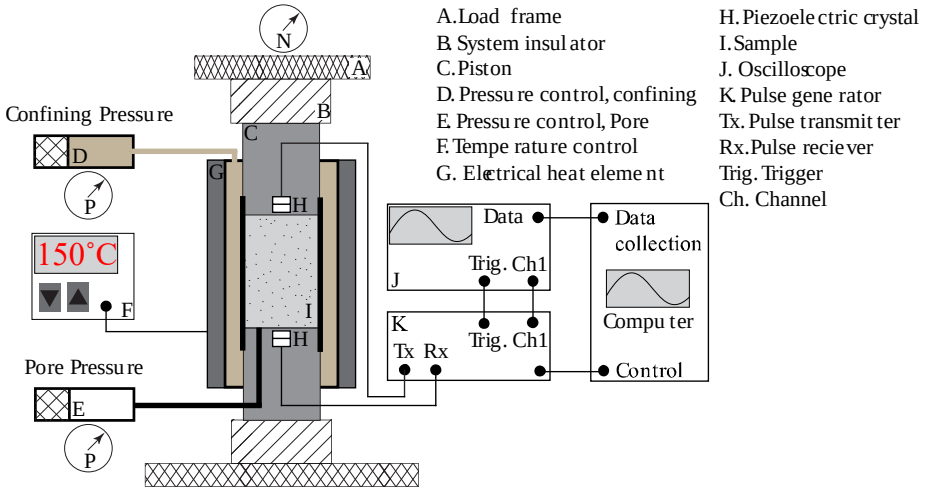

Figure III.2. Sketch of temperature controlled experimental setup for rock mechanical testing.

High temperature testing

The high temperature testing was separated branches of stiffness and strength. In the stiffness branch (Branch 2) where the axial stress kept below 15 MPa and samples subjected to loops of respectively hydrostatic as well as triaxial stress symmetry and a stepwise temperature increase of ambient 50°C, 100°C, 150°C and ≈170°C (Figure III.3). Deformation and ultrasonic velocities were during testing continuously recorded. Initiated directly subsequent to Branch 1, were samples in Branch 2 at in-situ temperature hydrostatically loaded to respectively 0.7, 3, 10 or 20 MPa where the confining stress was kept constant and axial stress increase until mechanical failure with continuously recorded axial deformation and ultrasonic velocities.

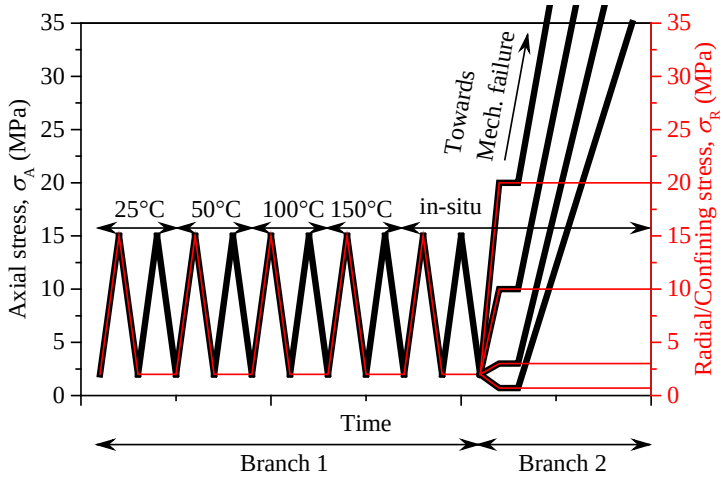

Figure III.3. Sketch of temperature controlled experimental setup for rock mechanical testing.

Industrial interest in the exploration of deep petroleum reservoirs and geothermal energy calls for increased theoretical and experimental knowledge on sedimentary rocks at elevated temperature. Sandstone is one class of sedimentary rocks both industries are targeting. Physical understanding of temperature effects on mechanical properties as well as the governing characteristics of heat transfer in sandstones may be significant for the industrial success, and for this reason the main research topics of this study.

DTU Civil Engineering
Technical University of Denmark

Brovej, Building 118
2800 Kongens Lyngby

www.byg.dtu.dk

ISBN 9788778775009
ISSN 1601-2917